Geotextiles and Geomembranes 39 (2013) 78–102

Contents lists available at SciVerse ScienceDirect

Geotextiles and Geomembranes

journal homepage: www.elsevier.com/locate/geotexmem

An analytical model for arching in piled embankments☆

S.J.M. van Eekelen [a,b,*], A. Bezuijen [a,c], A.F. van Tol [a,b]

[a] Deltares, Unit Geo-Engineering, P.O. Box 177, 2600 MH Delft, The Netherlands
[b] Delft University of Technology, The Netherlands
[c] Ghent University, Belgium

ARTICLE INFO

Article history:
Received 7 February 2012
Received in revised form
22 May 2013
Accepted 4 July 2013
Available online 16 August 2013

Keywords:
Load transfer platforms
Arching
Piled embankments
Soil reinforcement
Concentric arches model
Analytical models

ABSTRACT

Most analytical models for the design of piled embankments or load transfer platforms with geosynthetic reinforcement (GR) include two calculation steps. Step 1 calculates the arching behaviour in the fill and step 2 the load-deflection behaviour of the GR. A calculation method for step 2 based on the results of model tests has been published by Van Eekelen et al. (2012a,b). The present paper analyses and presents a new model for step 1, which is the arching step. Additional tests, which are also presented in this paper, were conducted for this purpose.

The new model is a limit-state equilibrium model with concentric arches. It is an extension of the models of Hewlett and Randolph (1988) and Zaeske (2001). The new model results in a better representation of the arching measured in the experiments than the other models mentioned, especially for relatively thin fills.

Introducing GR in a piled embankment results in a more efficient transfer of load to the piles in the form of an arching mechanism. The load is then exerted mainly on the piles and the GR strips between the piles, on which the load is approximately distributed as an inverse triangle. The new model presented in this paper describes this behaviour and is therefore meant to describe the situation with GR. The new model provides a physical explanation for observations of the arching mechanism, especially the load distribution on the GR. Other observations with which this model concurs are the dependency on fill height and friction angle. The amount of arching increases with increasing subsoil consolidation and GR deflection. The paper describes how the new model relates to the development of arching as a result of subsoil consolidation.

1. Introduction

Many analytical design models for the design of piled embankments include two calculation steps. The first step calculates the arching behaviour in the fill. This step divides the total vertical load into two parts: load part *A*, and the 'residual load' (*B* + *C* in Fig. 1). Load part *A*, called 'arching *A*' in the present paper, is the part of the load that is transferred to the piles directly.

The second calculation step describes the load-deflection behaviour of the geosynthetic reinforcement (GR, see Fig. 1). In this calculation step, the 'residual load' is applied to the GR strip between each pair of adjacent piles and the GR strain is calculated. An implicit result of step 2 is that the 'residual load' is divided into a load part *B* which passes through the GR to the piles, and a part *C* resting on the subsoil, as indicated in Fig. 1.

Van Eekelen et al. (2012b) analysed and made proposals for calculation step 2. The present paper analyses and puts forward a new model for step 1, the arching step. Both papers compare the results with measurements from a model test series presented in the first part (Van Eekelen et al., 2012a) of this three-part study. These tests are particularly suitable for the validation of calculation steps 1 and 2 separately because *A*, *B* and *C* were measured separately. For the present paper, a number of additional tests were carried out with the same test set-up.

Several families of analytical models describing step 1 (arching) are available in the literature. Terzaghi (1943) listed a number of them. Current arching models comprise:

Rigid arch models, such as several Scandinavian models (Carlsson, 1987; Rogbeck et al., 1998, modified by Van Eekelen et al., 2003; Svanø et al., 2000) and the Enhanced Arching model (also called the Bush–Jenner model or the Collin, 2004 model) and the present design method of the Public Work

* Corresponding author. Deltares, Unit Geo-Engineering, P.O. Box 177, 2600 MH Delft, The Netherlands. Tel.: +31 88 335 72 87.
E-mail address: suzanne.vaneekelen@deltares.nl (S.J.M. van Eekelen).

0266-1144/$ – see front matter © 2013 The Authors. Published by Elsevier Ltd. All rights reserved.
http://dx.doi.org/10.1016/j.geotexmem.2013.07.005

Nomenclature

A	load part transferred directly to the pile ('arching A' in this paper) expressed as kN/pile = kN/unit cell, kN/pile
$A\%$	arching A presented as a percentage of the total load, A % is the same as the pile efficacy ("E") as used by several authors: $A\% = E = 1 - \frac{B+C}{A+B+C}$ or $A\% = E = \frac{A}{A+B+C} = \frac{A}{(\gamma H+p)\cdot s_x \cdot s_y}$, %
a	width of square pile cap. $B_{ers} = a$, m
B	load part that passes through the geosynthetic reinforcement (GR) to the pile expressed as kN/pile = kN/unit cell, kN/pile
B_{ers}	equivalent size of circular pile cap, $B_{ers} = 1/2 \cdot d \cdot \sqrt{\pi}$ or the width of a square pile cap, m
C	load part that is carried by the soft soil between the piles (this soft soil foundation is called 'subsoil' in this paper) expressed as kN/pile = kN/unit cell, kN/pile
C	a constant to be calculated with boundary conditions (Eqs. (29)–(34) and (47)–(50) in the appendix)
d	diameter circular pile (cap), m
E	pile efficacy, the same as $A\%$, – (kN/kN)
F	force, kN
GR	geosynthetic reinforcement
h or H	height of the fill above bottom layer of GR, m
H_{g2D}	height of the largest of the 2D arches of the new concentric arches model, see Eqs. (2) and (13) and Figs. 10 and 12. H_{xg2D} refers to the height of a 2D arch that is oriented along the x-axis (perpendicular to the road axis), as indicated in Fig. 12. H_{yg2D} refers to the height of a 2D arch that is oriented along the y-axis, m
H_{g3D}	height of the largest 3D hemisphere of the new concentric arches model, see Eq. (4) and Fig. 10, m
h_g	arch height in EBGEO, $h_g = s_d/2$ for $h \geq s_d/2$ or $h_g = h$ for $h < s_d/2$, m
$J_{2\%}$	tensile stiffness of the GR at a GR strain of 2%, kN/m
k	subgrade reaction, kN/m^3
K_p	passive or critical earth pressure coefficient, –
L_{x2D}	part of the GR strip that is oriented along the x-axis (perpendicular to the road axis) and on which the 2D arches exert a force, see Fig. 23 and Eq. (12), m
L_{y2D}	part of the GR strip that is oriented along the y-axis (parallel to the road axis) and on which the 2D arches exert a force, see Fig. 23 and Eq. (12), m
L_{x3D}	width of square on which the 3D hemispheres exert a load, see Fig. 22 and Eq. (8), m
P_{2D}	calculation parameter given by Eq. (1). P_{x2D} refers to a 2D arch that is oriented along the x-axis, as indicated in Fig. 12 and Eq. (14). P_{y2D} refers to a 2D arch that is oriented along the y-axis, kPa/m$^{K_p-1}$
P_{3D}	calculation parameter given by Eq. (7), kPa/m$^{2K_p-2}$
p	uniformly distributed surcharge on top of the fill (top load), kN/m^2
Q_{2D}	calculation parameter given by Eq. (1), kN/m^3
Q_{3D}	calculation parameter given by Eq. (7), kN/m^3
r	radius of a 2D arch, m
R	radius of a hemisphere (in this paper a hemisphere is a 3D arch), m
R_b	total friction between fill/box walls and foam cushion/box walls and piles, see Van Eekelen et al. (2012a,b), kN/pile
s_d	the diagonal centre-to-centre distance between piles $s_d = \sqrt{s_x^2 + s_y^2}$, m
s_x, s_y	pile spacing perpendicular to the road axis (x) or parallel to the road axis (y), m
W_n	net load ($= W_s - C - R_b$), kN/pile
W_s	total surcharge load on a unit area $W_s = p \cdot s_x \cdot s_y$, kN/pile
z	distance along the vertical axis as indicated in, for example, Fig. 3, m
φ	internal friction angle, °
γ	fill unit weight, kN/m^3
σ_r	radial stress in a 2D arch, kPa
σ_R	radial stress in a 3D hemisphere, kPa
σ_θ	tangential stress in 2D arch or 3D hemisphere, kPa
PET	polyester
PP	polypropylene
PVA	polyvinyl alcohol

Research Center in Japan (2000, discussed in Eskişar et al. 2012). In this class of models, it is assumed that an arch is formed that has a fixed shape. The shape of the arch is usually 2D or 3D triangular. It is assumed that the entire load above the arch, including the soil weight and the traffic load, is transferred directly to the piles (load part *A, or arching A*, see Fig. 1). The weight of the soil wedge is carried by the GR + subsoil (B + C). These models do not consider the mechanical properties of the fill, such as the friction angle, in their equations and they are therefore not discussed further in the present paper.

In equilibrium models, an imaginary limit-state stress-arch is assumed to appear above the GR + soft subsoil between the stiff elements. In the 3D situation, these stiff elements are piles; in the 2D situation, they are beams or walls. The pressure on the GR + subsoil ($B + C$) is calculated by considering the equilibrium of the arch. In most models, the arch has a certain thickness.

Two limit-state equilibrium models are frequently used in piled embankment design today. One of them is the Hewlett and Randolph model (1988), explained in Fig. 2, which was adopted in the French ASIRI guideline (2012) and suggested in BS8006 (2010) as an alternative for the original empirical model in BS8006. The other frequently used equilibrium model is Zaeske's model (2001, and also described in Kempfert et al., 2004), which is explained in Fig. 3. This model was adopted in the German EBGEO (2010) and the Dutch CUR226 (2010, described in Van Eekelen et al., 2010), and we refer to it here as 'EBGEO'.

Another family of arching models is the family of frictional models. Several authors have adopted the frictional model proposed by Terzaghi (1943), who in turn based his model on previous work from other authors such as Cain (1916) and Völlmy (1937). McKelvey (1994) extended Terzaghi by assuming that a 'plane of equal settlement' exists and combined this with a tensioned membrane theory.

Russell and Pierpoint (1997) extended the Terzaghi model to include a third dimension by assuming the presence of friction in the vertical planes along the edges of the square pile caps. McGuire et al. (2012) also adopted the idea of a 'plane of equal settlement', which they described as the 'critical height'. They conducted numerous tests and collected field data to determine and validate their equation for the critical height. This critical

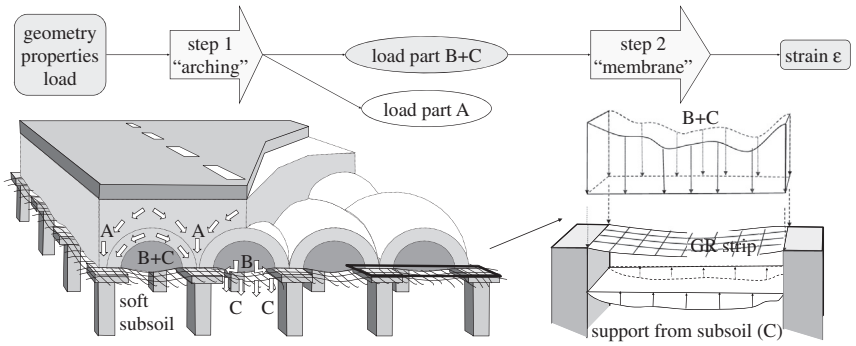

Fig. 1. Calculating the geosynthetic reinforcement (GR) strain comprises two calculation steps.

height should be used in combination with Russell and Pierpoint's (1997) version of Terzaghi (1943).

Naughton (2007) determined the critical height with log spiral shear planes. Britton and Naughton (2008) presented 3D experiments validating the critical height of this model.

Although the ideas underlying the frictional models are extremely important, these models are not generally used in Europe for piled embankment design and they will not be discussed further. A possible reason for the infrequent use of these models in Europe is that the results depend to a large extent on the value of K_0 (the ratio between horizontal and vertical pressure) and the fact that it is difficult to determine an accurate value for K_0.

Other examples of models considered in the literature are the models using mechanical elements, like the load displacement compatibility method of Filz et al. (2012), the one-dimensional model of Chen et al. (2008) and the plane strain models of Deb (2010), Deb and Mohapatra (2012) and Zhang et al. (2012). Filz et al. (2012) model the fill, the GR and the piles + subsoil as separate elements. The boundary condition for each of the elements is that deformation must match neighbouring elements. This determines the load transferred to the piles directly (arching *A*, see Fig. 1). Filz et al. (2012) limit arching *A* with 3D Terzaghi (cross-shaped, according to Russell and Pierpoint, 1997), plus critical height.

A familiar empirical model is the modified Marston and Anderson model (1913) that was modified by Jones et al. (1990) and adopted in BS8006 and the Finnish design guideline (Liikennevirasto, 2012). Marston and Anderson (1913) carried out numerous experiments to determine arching above a pipe in soil. They found a 2D equation that was modified by Jones et al. (1990) for the 3D piled embankments, as explained and further modified in Van Eekelen et al. (2011). This model is very important because of the widespread application of BS8006.

The final type of model that should be mentioned is the family of hammock models, such as the 'path of minor principal stress' model described by Handy (1985).

Most step 1 models calculate one average pressure on the GR. EBGEO uses, in its step 2, a triangular pressure distribution. This is an assumption following from Fig. 9.15 of EBGEO (2010), not the result of a calculation. Van Eekelen et al. (2012a,b) showed that the measured pressure distribution on the GR strip between the piles can be better approximated with an 'inverse triangle'.

The present paper presents a new equilibrium model for step 1 that is a better match for several experimental, numerical and field observations, particularly the measured inverse triangle in the pressure distribution. The starting point for this study consisted of the design models in general use in Europe. The new model is an extension of the Hewlett and Randolph (1988) and EBGEO (2010) models.

2. Additional laboratory tests

2.1. Measurements of steps 1 and step 2 separately

Van Eekelen et al. (2012a) presented and analysed a series of twelve model laboratory model tests on piled embankments. Since then, eight additional model tests have been carried out with the same set-up. Six of them were carried out specifically to validate variations in calculation step 1. These tests are presented here. One of the strengths of the test set-up was that it was possible to validate calculation steps 1 and 2 (Fig. 1) separately because the values of *A*, *B* and *C* are measured separately.

2.2. Description tests

Fig. 4 shows the test set-up for both the first and the second series, except for two additional total pressure cells (TPCs), which

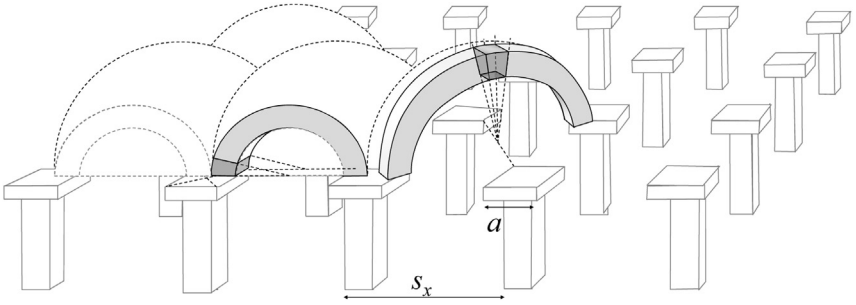

Fig. 2. Hewlett and Randolph (1988) consider the 'crown' element of the diagonal arch and the 'foot' element (just above the pile cap) of the plane strain arch as indicated in this figure.

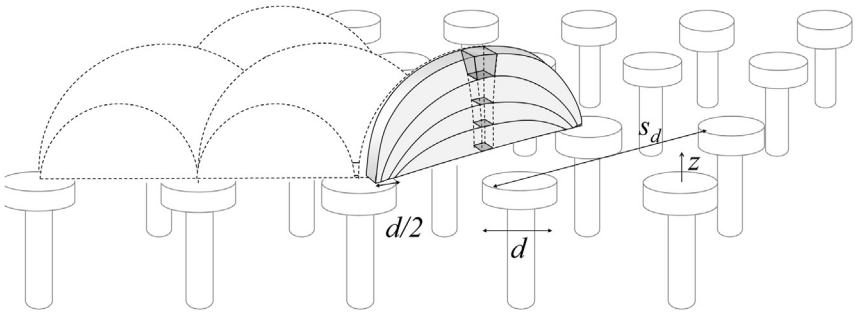

Fig. 3. Zaeske (2001) considers the equilibrium of the crown elements of the diagonal arches.

were used in the second series only. The insides of the box walls were located on the lines of symmetry. A foam cushion modelled the soft soil around the four piles. This cushion was a saturated and watertight sealed foam rubber cushion. A tap allowed drainage of the cushion during the test to model the soft-soil consolidation process. A stiff steel frame was installed to which the GR was attached. The steel frame could move freely in a vertical direction. Since it fitted precisely in the container, no horizontal movement was possible. Differential settlement along the frame bars was not possible. It is assumed that this has a negligible influence on differential settlement between the piles.

The embankment in most tests was granular fill (crushed recycled construction material 1–16 mm, $\varphi = 49^\circ$ at a unit weight of 16.4 kN/m^3). The friction angle $\varphi = 49^\circ$ of the granular fill was measured in large diameter ($\varnothing = 0.3$ m) triaxial tests. The average relative density in the triaxial tests and scale model tests was nearly the same at 61.0% and 62.9% respectively. The top load was applied with a water cushion that made it possible to apply stresses comparable with field stresses.

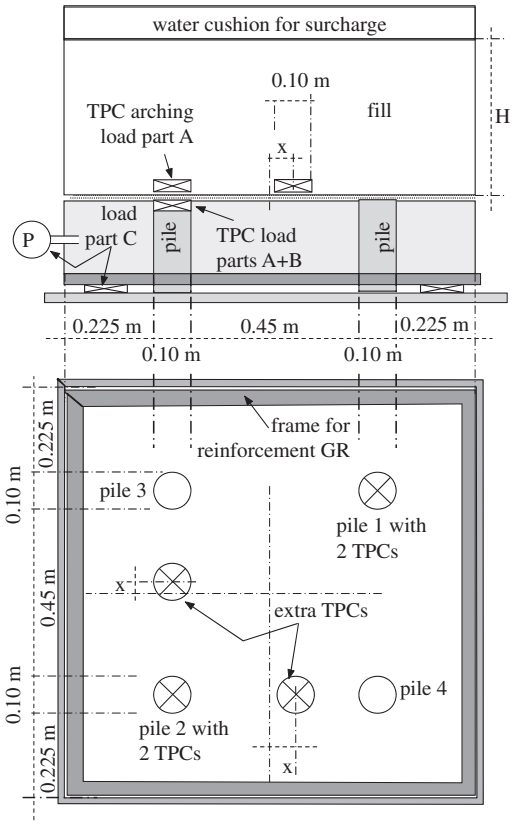

Fig. 4. Test set-up for piled embankment model experiments. The stress distribution is measured with total pressure cells (TPCs). See also Van Eekelen et al. (2012a), which includes an extensive presentation of the test series, including measurements of strains and deformations.

The area replacement ratio $a^2/(s_x \cdot s_y)$ in the test series described was 2.6%, while the area replacement ratio in Dutch practice is between 4.5 and 12%. This was a deliberate decision with the aim of generating enough GR tensile forces at this smaller scale.

After the introduction of the fill, each test was carried out as follows: (1) one drainage step foam cushion (subsoil consolidation), (2) first top load increment, (3) one or more drainage steps (4) second top load increment, (5) one or more drainage steps and so on, up to the maximum top load (varying between 50 and 100 kPa) and the subsequent drainage steps. The test concluded with the complete removal of the subsoil support by applying vacuum to the foam cushion.

Table 1 lists a selection of the tests in the first series, and all the tests in the new second series presented in the present paper. The tests from the second series are all variations on test K2, except that each test included one variation, which is indicated in bold in Table 1. Furthermore, additional total pressure cells were added to measure the load distribution on the GR strips.

The GR in these additional tests consisted of two layers of woven PVA grid, except for test K7, where the bottom layer was replaced by a similar PVA geotextile. The two uniaxial reinforcement layers were placed directly upon each other on one frame. The strength direction of one geogrid was perpendicular to the other. There was no distance between these two GR layers. The two layers are therefore considered to be a single GR layer that is completely biaxial.

GR stiffness depends on GR strain and the duration of loading, as well as other factors. The stiffness values of the weak direction of one GR layer and the stiff direction of the other layer were aggregated, resulting in a total GR stiffness $J_{2\%} = 2269$ kN/m in each direction. $J_{2\%}$ is the GR stiffness for a GR strain of 2%, and is determined in accordance with ISO 10319. These ISO tests are much faster than the piled embankment model tests (that took 3 days each). This means that the GR in the model tests is loaded longer and will behave differently (less stiffly) from the behaviour suggested by this $J_{2\%}$. However, GR stiffness is not a parameter in analytical step 1: the arching calculations considered in the present paper. Van Eekelen et al. (2012a) confirmed that using GR has a major impact on the arching mechanism, but GR stiffness (as long as the stiffness complies with a good-quality design model) does not have a measurable influence.

Table 1
Specification of the additional series 2 scaled model tests, and a selection of the series 1 tests. The series 2 tests were a variation on test K2 presented in Van Eekelen et al. (2012a).

Sequence of tests	Code	GR $J_{2\%}$ = 2269 kN/m except tests T2 and T3	Fill height granular fill $\varphi = 49.0°$ except test T2	Fill unit weight	Top load p[a]
			m	kN/m^3	kPa and kN/pile
Selection of tests of series 1 (Van Eekelen et al., 2012a)					
6	K2	2× PVA grid	0.420	16.59	p = 0–25–50–75–100 kPa (= 0–7.6–15.1–22.7–30.2 kN/pile) p–R = 1.2–22.0–41.1–59.8–74.9 kPa
5	T2	**1× PP geotextile J2% = 970/1810 kN/m**	0.420 sand $\varphi = 40.9°$	16.55	p = 0–25–50–75 kPa (= 0–7.6–15.1–22.7 kN/pile) p–R = −1.8–18.3–37.4–50.9 kPa
7	T3	**1× PP geotextile J2% = 970/1810 kN/m**	0.420	16.70	p = 0–25–50–75 kPa (= 0–7.6–15.1–22.7 kN/pile) p–R = −0.2–19.7–39.0–55.2 kPa
Series 2					
13	K4	2× PVA grid	**0.655**	16.80	p = 0–25–50–75 kPa (= 0–7.6–15.1–22.7 kN/pile) p–R = −0.9–13.9–28.5–44.7 kPa
14	K5	2× PVA grid	**0.343**	17.95	p = 0–25–50–75–100 kPa (= 0–7.6–15.1–22.7–30.2 kN/pile) p–R = −2.7–14.3–31.9–49.9–67.2 kPa
15	K6	2× PVA grid	0.429	16.35	**p = 0–50–100 kPa (= 0–15.1–30.2 kN/pile)** p–R = −1.3–31.7–66.1 kPa
16	K7	**Bottom layer PVA geotextile, top layer PVA grid**	0.426	16.42	p = 0–25–50–75–100 kPa (= 0–7.6–15.1–22.7–30.2 kN/pile) p–R = 0.0–17.3–33.9–51.4–68.0 kPa
17	K8	2× PVA grid	**0.227**	17.13	p = 0–25–50–75–100 kPa (= 0–7.6–15.1–22.7–30.2 kN/pile) p–R = −0.1–18.0–35.6–57.7–73.8 kPa
18	K9	2× PVA grid	**0.655**	16.82	p = 0–25–50–75–100 kPa (= 0–7.6–15.1–22.7–30.2 kN/pile) p–R = −4.8–12.4–28.6–43.5–63.8 kPa

[a] After each top load increase, controlled drainage of the foam cushion ('subsoil') follows in one or more steps until the subsoil support C is nearly gone. The calculations were carried out with surcharge load p–R, where R is the measured friction between fill and box walls. The listed p–R is given for the moments just before top load increase (and therefore for minimal subsoil support C).

2.3. Results of the additional tests

Fig. 5 compares the measurements of arching A in the new model tests with several old model tests. The numbers between brackets refer to the sequence of tests.

The granular fill was re-used for each test. It was observed that large numbers of grains were crushed during the successive tests. This will probably have caused a reduction of the friction angle. A lower friction angle results in less arching, as shown by the figure. Arching was also relatively low in test T2, in which a sand fill was used.

The friction angle $\varphi = 49°$ of the granular fill was measured with large triaxial tests carried out between experiments 12 and 13. This effect of reducing friction is neglected in the present paper. In the calculations, friction angle $\varphi = 49°$ was applied.

More results from the additional tests are presented in Figs. 7, 15, 17, 19 and 21 of this paper.

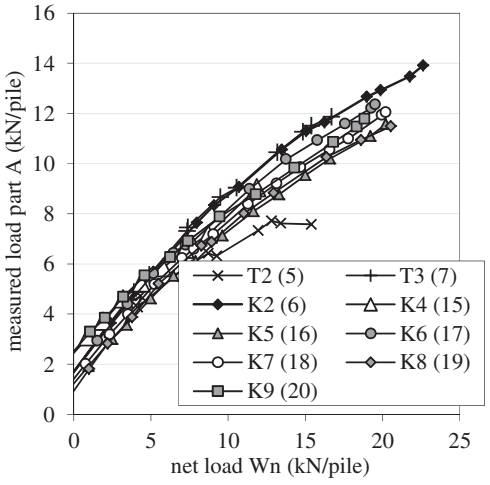

Fig. 5. Measurements of arching A in a selection of the experiments in series 1 (Van Eekelen et al., 2012a) and the additional tests in series 2. The numbers between the brackets refer to the sequence of tests.

3. Observations of arching in experiments, field tests and numerical calculations

3.1. Measuring arching

This paper focuses on the description of the arching mechanism, and therefore on calculation step 1 in Fig. 1. Arching divides the vertical load into two parts, as shown in Fig. 1. One part is load part A (called 'arching A' in this paper), which is the load that is transferred to the pile caps directly. The remaining load part is $B + C$.

Direct validation of arching in a GR reinforced piled platform with measurements is only possible when A is measured separately, as shown in Fig. 4. This figure shows how load A was measured in the tests, using total pressure cells (TPCs) with a diameter equal to the pile diameter. They were located on top of the piles and on top of the GR. In addition, two total pressure cells measured $A + B$. They were located below the GR on top of the piles. This paper gives arching A in kN/pile. In several figures, arching is presented as a percentage of the total load, which is referred to as "A%". A% corresponds to efficacy ("E") as used by several authors, where $E = A\% = A/(A + B + C)$, with A, B and C given in kN/pile, A% in % and E as a ratio (−).

Many researchers (such as Zaeske, 2001; Blanc et al., 2013) have measured $A + B$ or measured A in a piled platform without GR (Hewlett and Randolph, 1988; Ellis and Aslam, 2009, for example). As far as we are aware, only the Dutch research programme has reported measurements of A in experiments with GR (Van Eekelen et al., 2012a,b) and three field tests with GR (Van Duijnen et al., 2010; Van Eekelen et al., 2010; Van Eekelen and Bezuijen, 2012, 2013).

3.2. Comparison of predictions and measurements of arching A

Van Eekelen et al. (2012b) measured A in their experiment series and showed that EBGEO generally under-predicts the measured A. This paper presents additional tests of the same type. Van Duijnen et al. (2010) measured A in field tests under a railway in Houten, the

Netherlands. They showed that EBGEO considerably under-predicts *A*, as also shown in Fig. 16a.

More recently, Van Eekelen and Bezuijen (2013) showed that EBGEO only slightly under-predicts *A* as a result of the permanent load in field measurements in Woerden, the Netherlands, as shown in Fig. 16b.

It should be noted that the results of the predictions are highly dependent on the friction angle of the fill and that this friction angle is difficult to determine in the field. The presented EBGEO prediction for Woerden, for example, is calculated with a best-guess friction angle $\varphi = 43°$, resulting in $A = 113$ kN/pile, as indicated in Fig. 16b. However, this EBGEO-prediction of *A* falls to 96 kN/pile for $\varphi = 37.5°$ and rises to 132 kN/pile for $\varphi = 49°$.

It is also not certain that this friction angle or cohesion remains constant in all circumstances, such as heavy rain or long dry, hot periods: the arching in Fig. 16b increased in the spring of 2011 during a dry, hot period.

3.3. Impact of fill height

Several researchers have reported that the efficiency of arching increases with increasing fill height. Examples are Chen et al. (2008) in 2D experiments with GR and Zaeske (2001) with 3D experiments (although the latter only showed the differences in his experiments without GR), Han and Gabr (2002) with numerical analysis with GR, Le Hello and Villard (2009) with numerical analysis with GR (see Fig. 18), Jenck et al. (2009) with 2D experiments without GR and numerical analysis, Ellis and Aslam (2009) with centrifuge tests without GR, and Deb and Mohapatra (2012) with 2D analytical calculations. All these researchers showed that a higher fill results in relatively more load being transferred to the piles, either directly or via the GR. A higher fill therefore results in a relative reduction in the load exerted on the GR and/or the subsoil between the piles.

The experiments presented in this paper also show that fill height has an impact, as seen in Fig. 17. *A%* increases with fill height and seems to stabilise with increasing embankment height, as shown in Figs. 17 and 18. When *A%* stabilises, the absolute values of *A* and $B + C$ (kN/pile or kPa) will increase with increasing fill height. This tendency towards increasing arching is followed by many design models, such as Carlsson (1987), Guido et al. (1987), Hewlett and Randolph (1988), Russell and Pierpoint (1997), Sintef (2002) and Kempfert et al. (2004), which was adopted in EBGEO (2010), as Le Hello and Villard (2009) have shown.

The critical height decreases with increasing fill height. The critical height is the height at which the shear forces in the embankment fill are reduced to zero (Naughton, 2007), which is the case at the 'plane of equal settlement' as defined by McKelvey (1994). Lally and Naughton (2012) carried out a series of 2D GR-reinforced centrifuge tests. They found close agreement between the observed critical heights and the critical height suggested by Hewlett and Randolph's model (1988).

3.4. Load distribution on the GR; influence of using GR

There is a considerable difference between piled embankments with or without GR. GR, when stiff enough, leads to (1) more efficient arching and therefore a higher *A*, (2) a concentration of load on the GR strips (3) an inverse triangular load distribution on the GR strips and (4) a larger fall in stress between the piles with depth in the embankment above the GR. Each of these features will be explained in this section.

Chen et al. (2008), Abusharar et al. (2009) and Deb and Mohapatra (2012) showed that the efficiency of the piled embankment improves greatly when GR is used. They found that the load on the piles was much larger with, respectively, a 2D analytical model, an axial-symmetric analytical model and in 2D experiments.

The localisation of the load on the GR strips has been shown by, for example, Zaekse (2001) by measuring the pressure at three locations on the GR square and the GR strips (Fig. 6). Note that, in this paper, the square between four piles is referred to as the 'GR square', even when no GR is in place, as indicated in Fig. 11. Fig. 6 shows that introducing GR clearly transfers the load towards the GR strips. This results in a load distribution that is concentrated mainly on the GR strips (and probably the piles, but Zaeske did not measure *A*). As a result, it is expected that the strains in the GR occur mainly in the GR strips between the piles. This was indeed found in both Zaeske (2001) and Van Eekelen et al. (2012b).

The pressure on the GR strips is not equally distributed; it rises towards the piles. In the additional tests presented in this paper, the load distribution on the GR strip was measured with additional total pressure cells on the GR strip (Fig. 4). These measurements (Fig. 7) do indeed show that the load on the GR rises towards the piles. This load distribution can be approximated by a model with an inverse triangular load distribution. The inverse triangular model has advantages since it is a relatively simple analytical model. Van Eekelen et al. (2012a,b) and Van Eekelen and Bezuijen (2013) showed that this simplified analytical model provides a good match with measurements of deformation in laboratory experiments. Furthermore, the inverse triangle (or at least the concentration of load close to the piles, and the minimum load in the centre between piles) was also found in, for example, finite element calculations on a soldier pile wall by Vermeer et al. (2001), discrete element calculations on a heap of grains on a deflecting subsurface (Nadukuru and Michalowski, 2012), numerical calculations by Han et al. (2012), with a inversed triangle in their Fig. 9, and by Den Boogert et al. (2012), settlement measurements in a field test (Van Eekelen and Bezuijen, 2012, 2013) and the large-scale model tests of Filz and Sloan (2013).

GR also has a major effect on ground pressure in the fill above the GR between the piles. Zaeske (2001, pages 55 and 63) showed that this ground pressure declines with increasing fill depth. When GR is applied, the fall in ground pressure with depth is much larger than without GR, as shown by the comparison of Zaeske's measurements in the situations with and without GR in Fig. 20.

Zaeske's findings (2001) showed that there is an interaction between the GR and the fill. Without GR, the arch is much less efficient than with GR. The GR attracts the load to the GR strips between the pile caps and then further to the pile caps, approximately resulting in the inverse triangular load distribution on the GR strips. This ultimately results in larger vertical loads on the pile caps and on the GR close to the pile caps. GR therefore makes arching much more efficient.

The current analytical models do not give the localisation of the load on the GR strips. Nor do they result in a concentration of load on the GR in the area around the pile cap or, therefore, lead to an inverse triangular load distribution. This paper describes a new equilibrium model that is a better match for load distribution observations. The resulting model is only applicable to load transfer platforms with GR.

3.5. Influence of subsoil consolidation or GR deflection and fill properties

1. Consolidation or compaction of the subsoil results in an increase of arching *A*, as shown by Van Eekelen et al. (2012a), and in Fig. 8. Most analytical models, like EBGEO, do not calculate with increased arching due to subsoil consolidation. An exception is the model of Deb (2010), which agrees with this influence of consolidation.

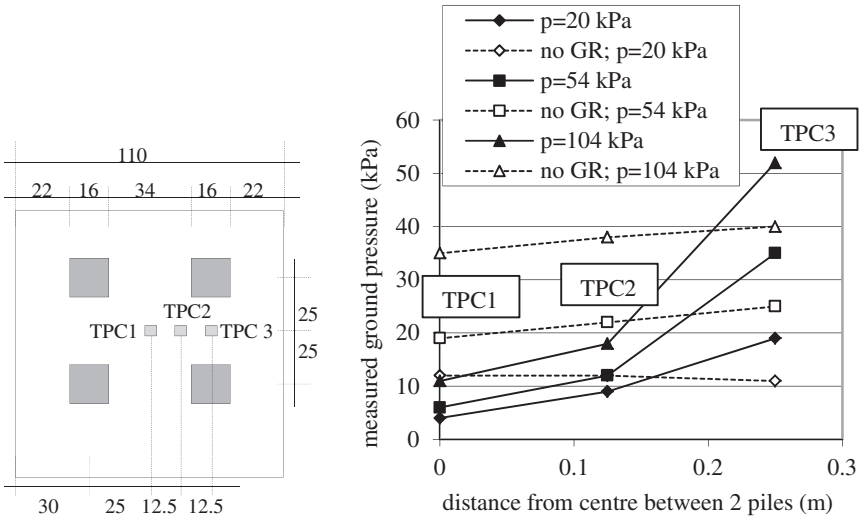

Fig. 6. Comparison of results of the Zaeske test series (2001, page 60, GR is a woven grid PET 60/60-20). Top view. Zaeske measured the load distribution at 5 cm above the GR, at the locations TPC1, TPC2 and TPC3. See also Fig. 20. Sizes in cm. $H = 0.7$ m, $\varphi_{fill} = 38°$.

2. A lower friction angle of the fill gives less arching during consolidation. This results in load part $B + C$ on the GR being some 39% larger for sand than for granular fill at the end of the tests presented by Van Eekelen et al. (2012a) and Fig. 8b.

Most of the existing arching models assume that a slight deflection of the geotextile is sufficient to create a 'full arch'. However, the measurements showed that A increases with increasing GR deflection (due to subsoil consolidation). The influence of deformation cannot be incorporated in rigid-plastic models such as the equilibrium models or frictional models. A new class of models would be needed. This would, however, conflict with the initial principle of keeping as closely as possible to existing design models, and it is beyond the scope of this paper. A 'work-around' is presented in section 4.2: the development of concentric arches.

3.6. Summation of section 3

Comparing the existing models with measurements, it can be concluded that none of the analytical models considered (equilibrium, frictional, empirical) can explain the measurements. In several cases, they under-predict the arching A measured in the field. They do not describe the load and strain localisation on and in the GR strips. They do not give an explanation for the approximately inverse triangular load distribution on the GR strips. However, they do give decreasing ground pressure with depth in the fill above the GR square, and they do give increasing efficiency in arching with increasing fill height.

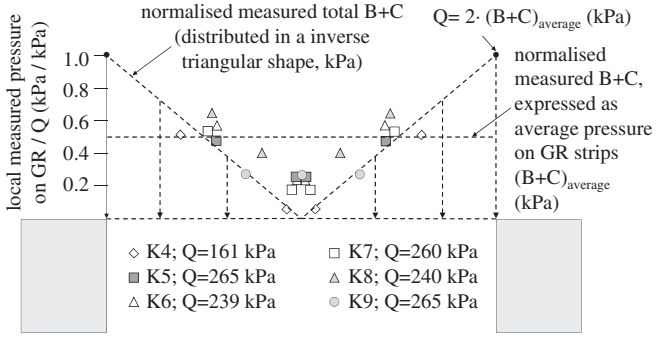

Fig. 7. Measured load distribution on GR in newly presented tests (Table 1) compared with the total measured load B + C on the GR, presented as an equally distributed load and with the inverse triangular load distribution of Van Eekelen et al. (2012a,b). The total measured B + C (kN/pile) was measured with the transducers that measure A, A + B and C indicated in Fig. 4. These values were divided by the area of a GR strip to get the equally distributed load $(B + C)_{average}$ in kPa. The local pressures were measured in kPa with the extra TPC's indicated in Fig. 4.

4. A new equilibrium model: the concentric arches model

4.1. Introduction

With equilibrium models, the pressure on the GR is calculated by considering the equilibrium of the arch. The models of Hewlett and Randolph (1988) and Zaeske (2001), which are in widespread use, are shown in Figs. 2 and 3. These two models give quite satisfactory results when used in a design (the predicted loading on the GR is reasonable and on the safe side), but (1) do not explain the concentration of load on the GR strip, (2) do not explain or derive an inverse triangular load distribution on the GR strips and (3) do not give increasing arching during subsoil consolidation. Furthermore, the Hewlett and Randolph model is not meant for arching with GR, and not particularly suitable for partial arching situations, which are situations where the fill or embankment is thinner than the full arch height, in other words when $H < s_d/2$. The Zaeske model can work with these low embankments.

This section introduces a new model, the concentric hemispheres model. This model accounts for increased arching with subsoil consolidation and finds load localisation on the GR strips. Furthermore, it gives a physical explanation for the inverse triangular load distribution and is therefore a better match for the observations in section 3.

However, in practical applications, a limit-state version of the model will be applied. In that case, the concentric arches model behaves in a rigid-plastic way and will no longer describe the influence of subsoil consolidation or deformation.

It should be noted that in this paper a hemisphere is a 3D arch as indicated in Fig. 13, and an arch is a 2D arch, as indicated in Fig. 12.

4.2. Development of concentric arches

Fig. 9 introduces a 2D picture of the new model that describes the development of arching during subsoil consolidation, accompanied by an increasing GR deflection.

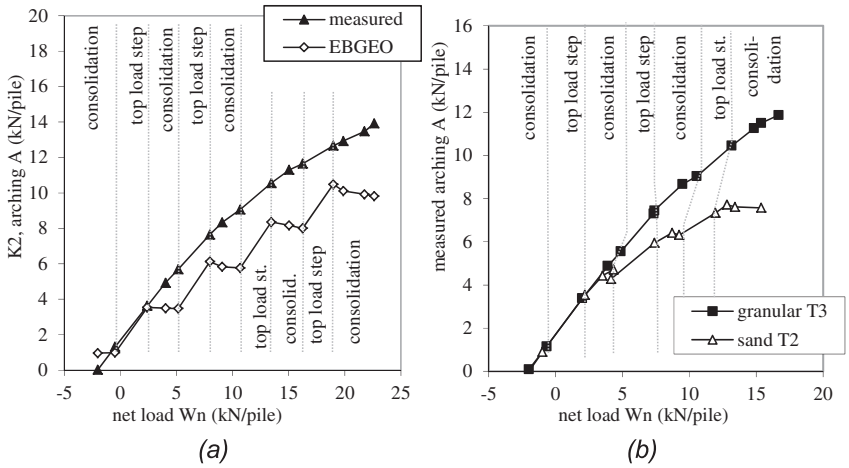

Fig. 8. Measurements showing that arching increases with subsoil consolidation (a): Comparison of measured and EBGEO calculations for test K2. (b): The increase in arching is larger for the stronger material 'granular' (test T3) than for sand (Test T2, source: Van Eekelen et al., 2012a, see Table 1 for specifications of tests K2, T2 and T3).

In Fig. 9a, a small GR deflection results in the start of arch formation at the edge of the pile cap. At this location (the edge of the pile cap), the differential settlement between GR and pile cap is at a maximum and the load starts to be attracted to the stiffer pile cap, resulting in an increasing pile load *A*. Subsequently, increasing GR deflection closes the arch (*b*).

Now, the piece of GR close to the pile behaves in a relatively stiff way because it is 'attached' to the pile and can move less freely than the GR in the middle. Another arch therefore starts to develop inside the first one (*c*). After this, more arches develop, each one smaller than the preceding one (*d*). Each smaller arch exerts a smaller force on its subsurface than the preceding larger arch. The arches give the directions of the main principal stresses: the major principal stress in the tangential direction and the minor principal stress in the radial direction.

The creation of new arches is accompanied by increasing load transfer in the direction of the piles and a reduction of the load on the GR area between the piles. This results in a more or less inverse triangular load distribution on the GR strip.

The process of arch development terminates in a set of concentric hemispheres which Fig. 10 shows in 3D. The GR is essential in this model because, without GR, there will be a more or less even settlement of the area between the piles and the concentric arches cannot develop, as shown with 2D experiments by for example Hong et al. (2007) and Jenck et al. (2009).

The development of arching in a basal reinforced piled embankment has never been observed through, for example, a glass wall. However, the formation of subsequent new concentric arches as a result of settlement underground has been observed in experiments at the University of Cambridge (Casarin, 2011). In these experiments, sand was poured onto a rubber tunnel. The largest differential settlements started, in this case, in the centre of the tunnel. In that case, a small arch in the fill occurred first, followed by a succession of larger arches.

The theory that base deflection results in concentric arches has also been stated by several authors presenting numerical analyses. For example, Han et al. (2012) carried out 2D DEM piled embankment analysis and showed (in their Fig. 11) force chains that resemble concentric arches, with smaller forces in the smaller arches. Vermeer et al. (2001) found main stress directions following concentric arches when they studied the horizontal stress distribution in the soil behind a soldier pile wall. A soldier pile wall of this

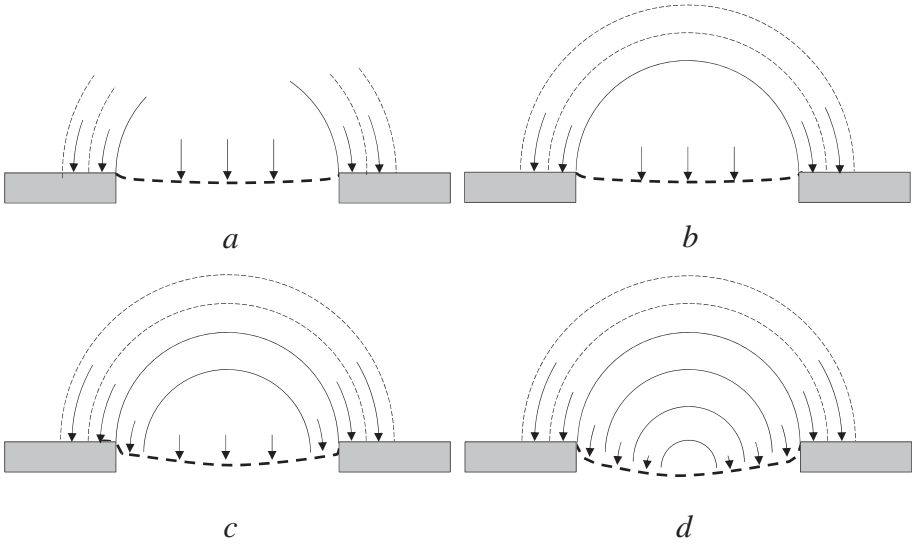

Fig. 9. Increasing GR defection results in an increasing lateral transport of load via concentric arch-shaped stress paths and an inverse triangular load distribution on the GR.

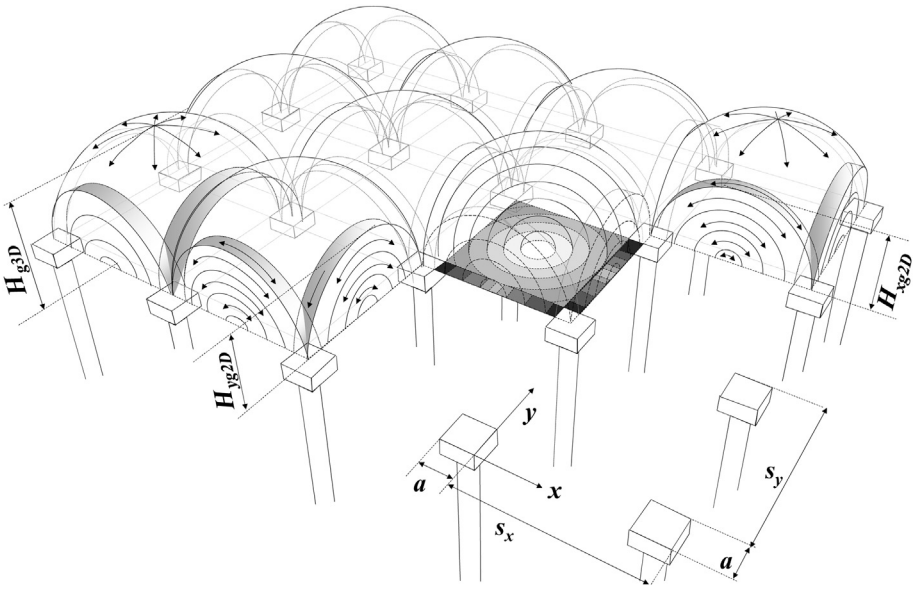

Fig. 10. New proposed analytical model: the concentric arches model. The load is transferred along the concentric 3D hemispheres towards the GR strips and then via the concentric 2D arches towards the pile caps.

kind consists of relatively weak timber laggings (comparable with GR) between stiff anchored steel piles (comparable with piles).

Another example is Nadukuru and Michalowski (2012), who carried out discrete element simulations. After a wedge-shaped heap of particles was formed, a basal deflection was prescribed. In this way, maximum subsidence at the centre equal to 0.67% of the heap's height was observed. Nadukuru and Michalowski showed their calculated force chains in the particles. The force chains follow the shapes of concentric arches. They also demonstrated that the load on the central part of the base was reduced in the process of deflection at the expense of the parts farther away from the centre. Each larger arch therefore exerts a larger stress on the base. This stress distribution resembles the inverse stress distribution presented in Van Eekelen et al. (2012a,b). Sloan (2011) also concluded from his large scale tests that it is possible that secondary arches form below the primary arch. His idea is similar to the concentric arches model presented in the present paper.

The new proposed model assumes that 3D concentric arches (hemispheres) are formed above the square between each four piles (Figs. 10 and 11b). These hemispheres transfer the load outward in all directions along the hemispheres towards the GR strips. The process continues with the further transfer of the load along the 2D arches above the GR strips towards the pile caps (Figs. 10 and 11c). Both the 3D hemispheres and the 2D arches exert a load on the GR subsurface which increases towards the outside. The part of the load not resting on the GR is arching A, which is the load part transferred directly to the pile caps, as explained in Fig. 11a. Fig. 11 depicts the three components of the model – (a) the load part (arching A) that is applied directly to the pile caps (Fig. 11a), (b) the load part that is applied on the GR square between the pile caps diagonally between the pile caps (Fig. 11b) and (c) the load part that is applied between adjacent pile caps on the GR strips (Fig. 11c) – plus the interaction that must exist between the last two components. With this model, it is possible to approximate the observed load distribution on the piles and the entire GR area between the piles.

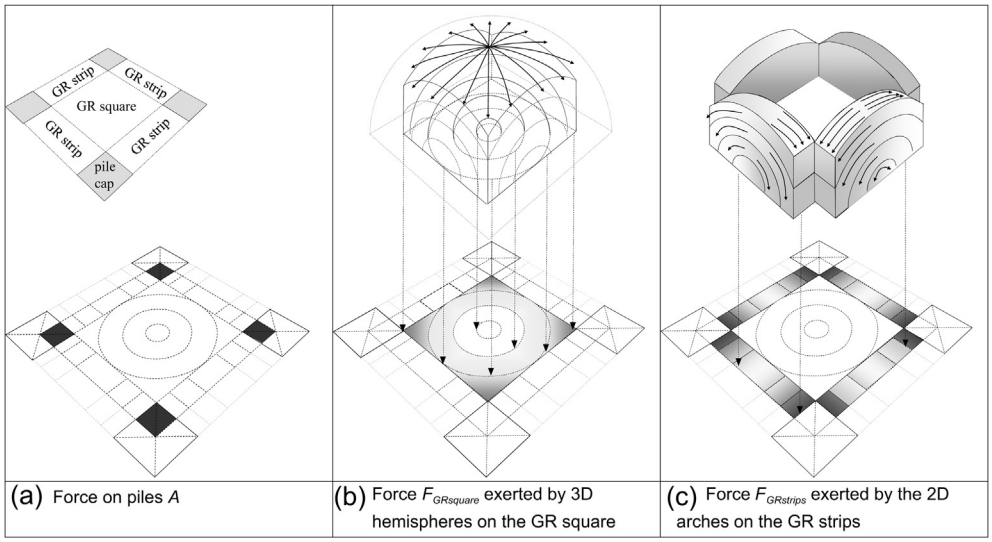

Fig. 11. Basic idea underlying the proposed concentric arches model: distribution of the load on the GR area between the piles and the determination of arching part $A = (\gamma H + p) \cdot S_x \cdot S_y - F_{GRsquare} - F_{GRstrips}$ going to the pile directly.

The following sections present the equations for the 2D concentric arches and the 3D concentric hemispheres and these 2D and 3D equations will then be combined to form the new arching model.

4.3. 2D concentric arches

Figs. 10, 11c and 12 show 2D concentric arches. It should be noted that this paper states the radius for 3D hemispheres as an upper-case R, and the radius of 2D arches as a lower-case r. The radial stress σ_r in the 2D arch is found by considering the radial equilibrium of the crown element of the 2D arch and assuming that the stress state in the arch is uniform around the semi-circle and that the limit state occurs in the entire arch, which gives the tangential stress $\sigma_\theta = K_p \cdot \sigma_r$. This leads, after some derivation given in Appendix A.1, to the following tangential stress (in kPa) for a 2D arch in the x-direction:

$$\sigma_\theta = P_{x2D} \cdot r^{(K_p-1)} + Q_{2D} \cdot r$$

$$\text{where } P_{x2D} = K_p \cdot H_{xg2D}^{1-K_p} \cdot \left[\gamma H + p - \gamma H_{xg2D} \frac{(K_p-1)}{(K_p-2)}\right] \quad (1)$$

$$\text{and } Q_{2D} = K_p \cdot \frac{\gamma}{K_p-2}$$

and, where H_{xg2D} (in m) is the height of the largest 2D arch (see Figs. 10 and 12):

$$H_{xg2D} = \frac{s_x}{2} \text{ for } H \geq \frac{s_x}{2} \text{(full arching)}$$

$$H_{xg2D} = H \text{ for } H < \frac{s_x}{2} \text{(partial arching)} \quad (2)$$

$$\text{and } K_p = \frac{1+\sin\varphi}{1-\sin\varphi}$$

The explanation of these equations is similar to Hewlett and Randolph's 2D explanation (1988), except that soil weight and top load are taken into account here. Hewlett and Randolph limit the thickness of their arch and therefore the crown element to half the width of a pile cap and calculate the vertical (radial) stress immediately below the crown element. For the concentric arches model, however, the arch is extended downwards towards the subsoil, resulting in a set of concentric arches. These arches exert a force on their subsurface, which comprises the GR strips, in the case of the 2D arches, as shown in Fig. 11c. The larger the arch, the larger the exerted force. This 'imprint' of load on the GR strip is shown in Fig. 12 and resembles the inverse triangle described in section 3.

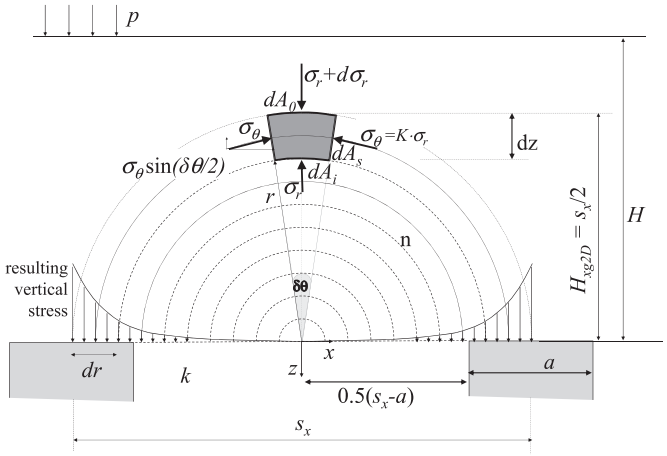

Fig. 12. 2D Concentric arches, the tangential stress in the arches result in a vertical stress exerted on the subsurface that resembles the simplified inverse triangle.

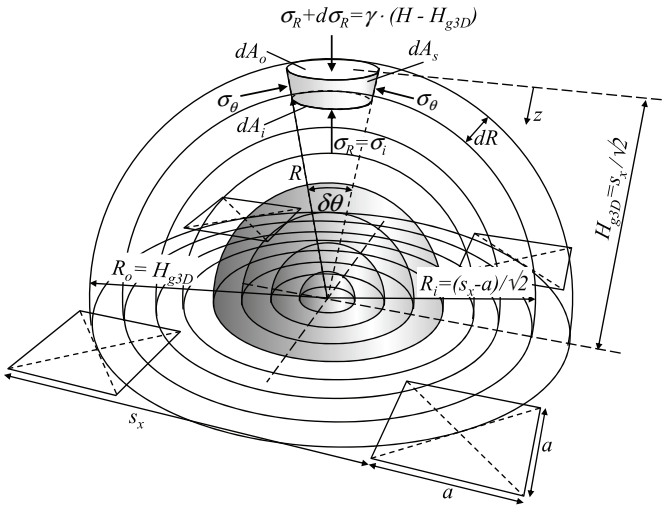

Fig. 13. 3D Concentric hemispheres, the tangential stress in the arches result in a vertical stress exerted on the subsurface.

4.4. 3D concentric hemispheres

Figs. 10, 11b and 13 show 3D concentric hemispheres. The tangential stress (kPa) in the 3D arches is found in a similar way as for the 2D arches, as explained in Appendix A.2:

$$\sigma_{\theta(p=0)} = P_{3D} \cdot R^{2(K_p-1)} + Q_{3D} \cdot R$$

$$\text{where } P_{3D} = \gamma \cdot K_p \cdot H_{g3D}^{2-2K_p} \cdot \left[H - H_{g3D} \cdot \left(\frac{2K_p-2}{2K_p-3}\right)\right] \quad (3)$$

$$\text{and } Q_{3D} = K_p \cdot \frac{\gamma}{2K_p-3}$$

and where K_p is given by Eq. (2) and H_{g3D} (m) by:

$$H_{g3D} = \frac{s_d}{2} \text{ for } H \geq \frac{s_d}{2} \text{(full arching)}$$

$$H_{g3D} = H \text{ for } H < \frac{s_d}{2} \text{(partial arching)} \quad (4)$$

With surcharge load p (kPa) the tangential stress (kPa) becomes (analogous to Hewlett and Randolph, 1988; Zaeske, 2001):

$$\sigma_\theta = \left(\frac{\gamma(H-z)+p}{\gamma(H-z)}\right)\left(P_{3D} \cdot R^{2(K_p-1)} + Q_{3D} \cdot R\right) \quad (5)$$

where z is the vertical distance between the considered point and the GR. So far, the explanation of the 3D equations is the same as Hewlett and Randolph's (1988). Hewlett and Randolph now limit the thickness of the arch and therefore the crown element to half the diagonal of a pile cap and calculate the vertical (radial) stress immediately below the crown element which gives Hewlett and Randolph's equation (10) (1988).

In the concentric hemispheres model, however, the arch is extended downwards towards the subsoil, resulting in a set of concentric hemispheres. These hemispheres exert a force on their subsurface. The larger the radius, the larger the force exerted on the subsurface.

4.5. Concentric arches model: combination of 2D arches and 3D hemispheres

The new calculation model is derived in Appendix A and summarised in this section. Note that the equations in the appendix are

for a situation in which the piles are placed in a grid with the same centre-to-centre distance in both directions: $s_x = s_y$, while this section extends the equations for the situation $s_x \neq s_y$. The model should be applied as follows:

1. Determine the total vertical load $F_{GRsquare}$ (in kN/pile) exerted by the 3D hemispheres on their square subsurface (Fig. 11b). This load $F_{GRsquare}$ is derived by integrating the tangential stress of the 3D hemispheres over the area of this square (see Appendix A.3 in Eq. (53)–(85)), resulting in:

$$\begin{aligned} F_{GRsquare} &= F_{GRsquare1} + F_{GRsquare2} + F_{GRsquare3} \\ &= \left(\frac{\gamma H + p}{\gamma H}\right) \cdot \left(F_{GRsq1p=0} + F_{GRsq2p=0} + F_{GRsq3p=0}\right) \end{aligned} \quad (6)$$

where

$$F_{GRsq1p=0} = \frac{\pi P_{3D}}{K_p} \cdot \left(\frac{L_{x3D}}{2}\right)^{2K_p} + \frac{2}{3}\pi Q_{3D} \cdot \left(\frac{L_{x3D}}{2}\right)^3$$

$$F_{GRsq2p=0} = {}_1F_{GRsq2} + {}_2F_{GRsq2} + {}_3F_{GRsq2} + {}_4F_{GRsq2}$$

where

$${}_1F_{GRsq2} = \frac{2\pi P_{3D}}{2K_p}\left(2^{K_p} - 1\right)\left(\frac{L_{x3D}}{2}\right)^{2K_p}$$

$${}_2F_{GRsq2} = \frac{2\pi Q_{3D}}{3}\left(\sqrt{2}^3 - 1\right)\left(\frac{L_{x3D}}{2}\right)^3$$

$$\begin{aligned} {}_3F_{GRsq2} &= \frac{P_{3D} \cdot 2^{2-2K_p} \cdot L_{x3D}^{2K_p}}{K_p} \cdot \left(-\frac{\pi}{2^{2-K_p}} + \sum_{n=0}^{\infty} \frac{1}{2n+1} \binom{K_p - 1}{n} \right) \\ &= \frac{P_{3D} \cdot 2^{2-2K_p} \cdot L_{x3D}^{2K_p}}{K_p} \cdot \left(-\frac{\pi}{2^{2-K_p}} + 1 + \tfrac{1}{3}(K_p - 1) \right. \\ &\quad + \tfrac{1}{10}(K_p - 1)(K_p - 2) \\ &\quad + \tfrac{1}{42}(K_p - 1)(K_p - 2)(K_p - 3) \\ &\quad + \tfrac{1}{216}(K_p - 1)(K_p - 2)(K_p - 3)(K_p - 4) \\ &\quad \left. + \tfrac{1}{1320} \ldots . (K_p - 5) \ldots \right) \end{aligned}$$

$${}_4F_{GRsq2} = \tfrac{1}{6} Q_{3D} L_{x3D}^3 \cdot \left(\sqrt{2}(1 - \pi) + \ln\left(1 + \sqrt{2}\right)\right)$$

where

$$P_{3D} = \gamma \cdot K_p \cdot H_{g3D}^{2-2K_p} \cdot \left[H - H_{g3D} \cdot \left(\frac{2K_p - 2}{2K_p - 3}\right)\right] \text{ and}$$

$$Q_{3D} = K_p \cdot \frac{\gamma}{2K_p - 3} \quad (7)$$

H_{g3D} (m) is the height of the largest hemisphere given in Eq. (4) and Fig. 10 and L_{x3D} is given by:

$$\begin{aligned} L_{x3D} &= \tfrac{1}{\sqrt{2}}\sqrt{(s_x - a)^2 + (s_y - a)^2} && \text{for } H \geq \tfrac{1}{2}\sqrt{(s_x - a)^2 + (s_y - a)^2} \\ L_{x3D} &= \sqrt{2} \cdot H_{g3D} && \text{for } H < \tfrac{1}{2}\sqrt{(s_x - a)^2 + (s_y - a)^2} \end{aligned} \quad (8)$$

where a (m) is the width of a square pile cap or the equivalent width of a circular pile cap and $F_{GRsquare}$ given in kN/pile. $F_{GRsquare1}$ and $F_{GRsquare2}$ (kN/pile) are indicated in Fig. 22. L_{x3D} (m) is the width of the square upon which the hemispheres exert a load, as indicated in Fig. 22.

When the area between the four piles $(s_x - a)\cdot(s_y - a) > L_{x3D}^2$, the area outside L_{x3D} but inside the GR square is assumed to be loaded by $\gamma H + p$. This gives an extra term, $F_{GRsq3p=0}$, where

$$\begin{aligned} F_{GRsq3p=0} &= \gamma H \cdot \left((s_x - a) \cdot (s_y - a) - L_{x3D}^2\right) && \text{for } L_{x3D}^2 < (s_x - a) \cdot (s_y - a) \\ F_{GRsq3p=0} &= 0 && \text{for } L_{x3D}^2 \geq (s_x - a) \cdot (s_y - a) \end{aligned} \quad (9)$$

The load that does not rest on the GR square is supposed to be transferred to the ring of GR strips and pile caps. This load is therefore applied as an equally distributed surcharge load on the 2D arches. This surcharge load on the 2D arches is in kN/pile:

$$\begin{aligned} F_{transferred} = \gamma H \cdot (s_x - a) \cdot (s_y - a) - \left(F_{GRsq1p=0} + F_{GRsq2p=0}\right. \\ \left. + F_{GRsq3p=0}\right) \end{aligned} \quad (10)$$

Distributed equally on the 2D arches, this results in a surcharge load in kPa (2 full GR strips and a pile cap per pile):

$$p_{transferred} = \frac{F_{transferred}}{a \cdot (L_{x2D} + L_{y2D}) + a^2} \quad (11)$$

where L_{x2D} is the length of the part of the GR strip upon which the 2D arches exert their force, as indicated in Fig. 23:

$$\begin{aligned} L_{x2D} &= s_x - a && \text{for } H \geq \frac{1}{2}(s_x - a) \\ L_{x2D} &= 2 \cdot H_{xg2D} && \text{for } H < \frac{1}{2}(s_x - a) \\ L_{y2D} &= s_y - a && \text{for } H \geq \frac{1}{2}(s_y - a) \\ L_{y2D} &= 2 \cdot H_{yg2D} && \text{for } H < \frac{1}{2}(s_y - a) \end{aligned} \quad (12)$$

and

$$\begin{aligned} H_{xg2D} &= \frac{s_x}{2} && \text{for } H \geq \frac{s_x}{2} \text{(full arching)} \\ H_{xg2D} &= H && \text{for } H < \frac{s_x}{2} \text{(partial arching)} \\ H_{yg2D} &= \frac{s_y}{2} && \text{for } H \geq \frac{s_y}{2} \text{(full arching)} \\ H_{yg2D} &= H && \text{for } H < \frac{s_y}{2} \text{(partial arching)} \end{aligned} \quad (13)$$

2. Determine the total load $F_{GRstrips}$ (kN/pile) on the GR strips. $F_{GRstrips}$ is derived by integrating the tangential load of the 2D arches over the area of the GR strips (see Appendix A.3 Eq. (86)–(91)), resulting in:

$$\begin{aligned} F_{GRstrip;p>0} &= \left(\frac{\gamma H + p}{\gamma H}\right) \cdot \left(2a \frac{P_{x2D}}{K_p}\left(\frac{1}{2}L_{x2D}\right)^{K_p} + \frac{1}{4} a Q_{2D} \cdot (L_{x2D})^2 \right. \\ &\quad + F_{xGRstr2p=0} + 2a \frac{P_{y2D}}{K_p}\left(\frac{1}{2}L_{y2D}\right)^{K_p} \\ &\quad \left. + \frac{1}{4} a Q_{2D} \cdot (L_{y2D})^2 + F_{yGRstr2p=0}\right) \end{aligned}$$

where

$$P_{x2D} = K_p \cdot H_{xg2D}^{(1-K_p)} \cdot \left[\gamma H + p_{\text{transferred}} - \gamma H_{xg2D} \cdot \left(\frac{K_p - 1}{K_p - 2}\right)\right]$$

$$P_{y2D} = K_p \cdot H_{yg2D}^{(1-K_p)} \cdot \left[\gamma H + p_{\text{transferred}} - \gamma H_{yg2D} \cdot \left(\frac{K_p - 1}{K_p - 2}\right)\right]$$

$$Q_{2D} = K_p \cdot \frac{\gamma}{K_p - 2}$$

$$F_{\text{xGRstr2}p=0} = \gamma H a (s_x - a - L_{x2D}) \quad \text{for } H < \frac{1}{2}(s_x - a)$$

$$F_{\text{xGRstr2}p=0} = 0 \quad \text{for } H \geq \frac{1}{2}(s_x - a)$$

$$F_{\text{yGRstr2}p=0} = \gamma H a (s_y - a - L_{y2D}) \quad \text{for } H < \frac{1}{2}(s_y - a)$$

$$F_{\text{yGRstr2}p=0} = 0 \quad \text{for } H \geq \frac{1}{2}(s_y - a) \tag{14}$$

and where L_{x2D} and L_{y2D} are given in Eq. (12). A practical limitation is a minimum embankment height of $H \geq 0.5 s_x$ and $H \geq 0.5 s_y$ so that the 2D arches always have enough height to develop fully. Furthermore, the largest 2D arches are wide enough to rest on the pile caps, as the width of the largest arch is equal to s_x or s_y. Fig. 14 shows that this requirement is not additional to EBGEO (2010) and CUR226 (2010) and only increases the minimum height in a limited, less realistic, number of cases for the British Standard (BS8006, 2010). However, the equations for the case $H < 0.5 s_{x,y}$ are stated here for calculations in the construction phase.

3. Determine the load distribution. The part transferred to the piles directly (arching A in kN/pile) is:

$$A = F_{\text{pile}} = (\gamma H + p) \cdot s_x \cdot s_y - F_{\text{GRsquare}} - F_{\text{GRstrips}} \tag{15}$$

as indicated in Fig. 11. The total load resting on GR + subsoil is therefore:

$$B + C = F_{\text{GRsquare}} + F_{\text{GRstrip}} \tag{16}$$

Calculation step 2 derives the GR strain from this load part B + C (Van Eekelen et al., 2012b). Appendix B gives a calculation example using the concentric arches model for step 1 and the inverse triangular load distribution for step 2 following Van Eekelen et al. (2012b).

4.6. Line-shaped foundations

The concentric 2D arches also apply in the 2D situation where the embankment is supported by line-shaped supporting elements, such as diaphragm walls or beams. The equations for this case are given in Appendix A.4.

When a 2D situation with line-shaped foundation is compared to its corresponding 3D situation with square pile caps (same centre-to-centre distance, same width of square pile caps and line foundation), the resulting average pressure on the GR is lower for the 2D situation than for the 3D situation. This is different from the model of Zaeske, that finds a slightly higher average pressure on the GR in the 2D case.

5. Comparison with laboratory experiments, field tests and numerical calculations

5.1. Introduction

Step 1 of the calculation model calculates the arching expressed in arching A, and also calculates the load distribution on the GR + subsoil. Both results of step 1 should concur with measurements, including the observed dependency on fill height and friction angle.

The calculations for this section have been carried out with the newly presented concentric-arches model described in section 4, EBGEO (2010) and Hewlett and Randolph (1988), all without safety factors.

Most of the presented experimental results are measurements during a minimum of subsoil support, in other words just before a top load increase in the experiments described in Section 2.

5.2. Arching A

Fig. 15 compares measured and calculated arching A of the experiments described in Section 2. Calculations that agree exactly with a measurement are located on the dotted diagonal line. The figure shows that the measurements agree much better with the concentric arches model than with EBGEO.

The concentric arches model has a better match than EBGEO for the embankments with a fill height of 0.34–0.42 m (K2, K5, K6, K7, T2 and T3, thus for $H/(s_d - d) = 0.51$–0.62). EBGEO under-predicts these measurements much more than the concentric arches model. These heights are important in design when making calculations for the construction phase. For the thinnest fill, K8, however, where $H/(s_d - d) = 0.33$, neither model works properly, but remains on the

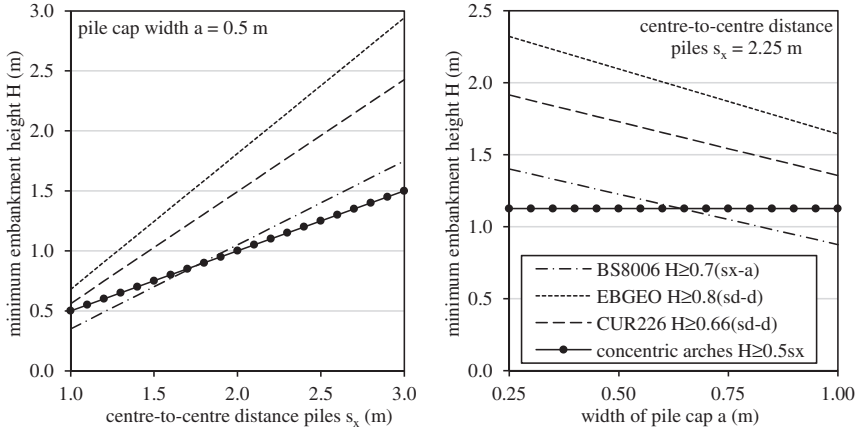

Fig. 14. Comparison of required minimum embankment heights for the new concentric arches model, BS8006 (2010), EBGEO (2010) and CUR226 (2010).

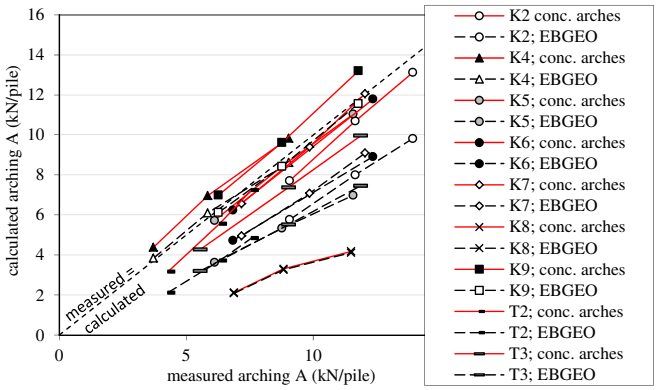

Fig. 15. Comparison of measured and calculated arching A in model experiments specified in Table 1.

'safe side' for the GR design: the models predict more load on the GR than measured.

It should be noted that EBGEO predicted the measurements for the thickest fills (K4 and K9, $H/(s_d - d) = 0.97$) very well. The concentric arches model, however, gives a slight over-prediction in cases with this relatively thick, but realistic, fill. However, in the following paragraphs, it is shown that measurements in two full-scale field tests, and numerical calculations with a full-scale geometry, produce a satisfying match with the results of the concentric arches model.

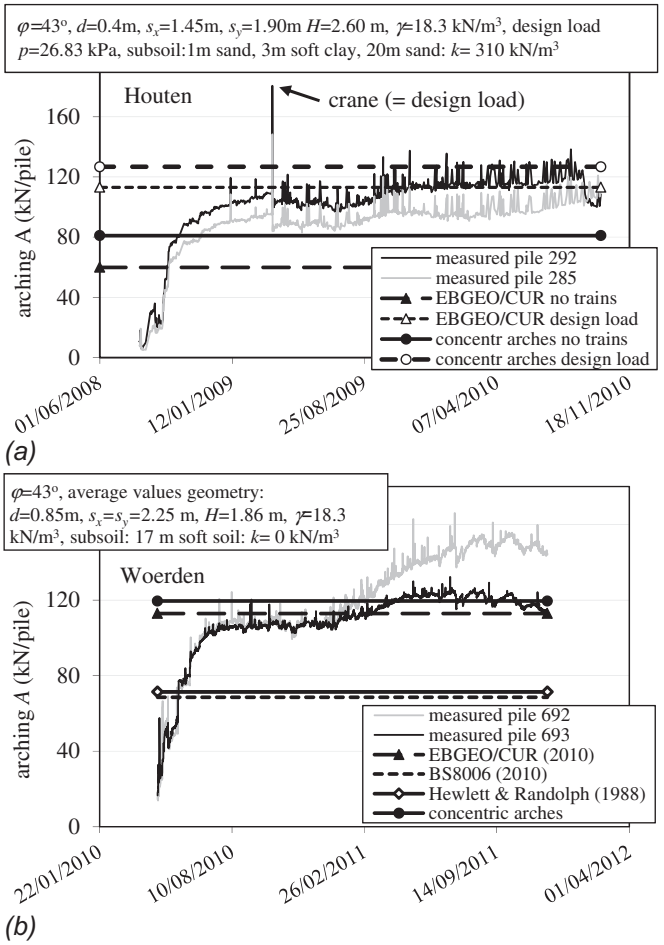

Fig. 16. Comparison of measured and calculated arching A in two field cases: (a) railway Houten, Netherlands, described in Van Duijnen et al. (2010) and (b) highway exit Woerden, Netherlands, described in Van Eekelen and Bezuijen (2012c). Prediction with surcharge load $p = 0$ kPa, see also Appendix B for a calculation example of this case.

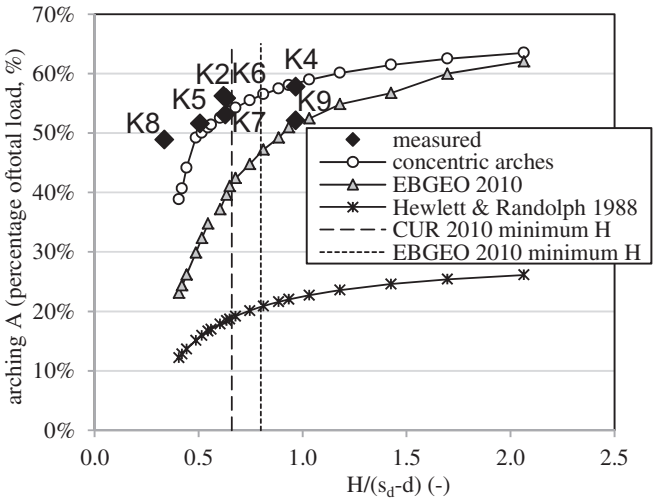

Fig. 17. Variation of embankment height H. Comparison of measured and calculated arching $A\%$ in model experiments specified in Table 1.

Fig. 16 compares full-scale field measurements with calculations. The figure shows that EBGEO and the concentric arches model agree better or equally well with the measurements. This is an important result, as it is dangerous to base the conclusions only on scaled model tests. It should be noted that it is difficult to determine the friction angle φ in the fill in the field, while even though φ has a major influence on the calculation results in each of the calculation models, as mentioned before in section 3.2.

5.3. The influence of fill height

Figs. 17 and 18 show the influence of embankment height H. Fig. 17 compares measurements of the model tests with predictions. The figure shows that the concentric arches model agrees better with the measurements than the other models. The figure shows that the measurements indicate that $A\%$ increases with embankment height and seems to stabilise for the higher embankments. This finding concurs with Le Hello and Villard's

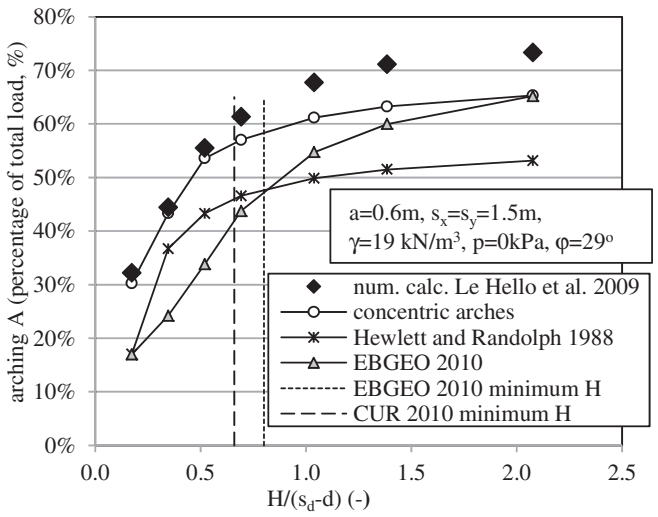

Fig. 18. Variation of embankment height H, comparison of analytical models with numerical calculations of Le Hello and Villard (2009).

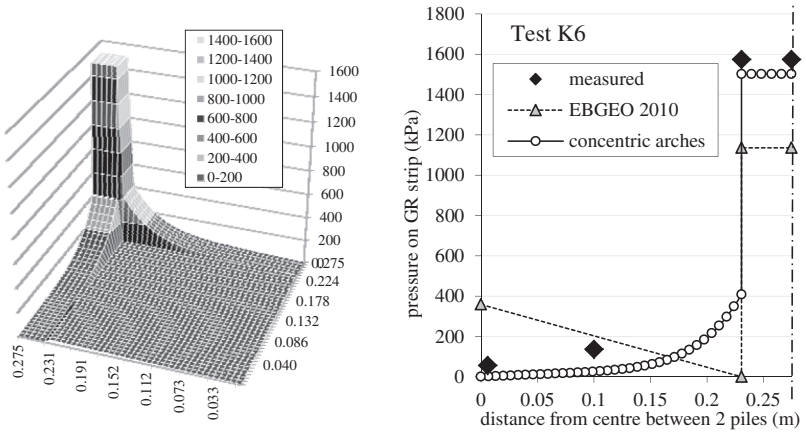

Fig. 19. Load distribution for test K6 for p-R_b = 66.1 kPa, which equals 20.0 kN/pile and minimum subsoil support: C = 0.5 kN/pile, (see Table 1). Left: load distribution calculated with concentric model in kPa. Right: cross-section through GR strip and pile. EBGEO gives an equally distributed load, which is translated in calculation step 2 into a triangular load distribution, which is given here.

numerical calculations (2009). They developed a numerical model that combined the 3D discrete element method and the finite element method. They also found increasing arching with fill height, stabilising for higher embankments. Fig. 18 shows that the concentric arches model is a reasonable match with the numerical calculations of Le Hello and Villard.

5.4. Load distribution on GR

Fig. 19 shows the measured and calculated load distribution on the GR strip. The figure presents the actual results from the new model. It is suggested that the step 2 calculations suggested in Van Eekelen et al. (2012b) should be followed for design purposes using the simplified inverse triangular load distribution.

The result of step 1 of EBGEO is pressure on a single point of the GR + subsurface. It is assumed that this pressure is the same everywhere between the pile caps, not only on the GR strip. This load is relatively low. For comparison purposes, the EBGEO pressure on GR + subsurface in Fig. 19 has been concentrated on the GR strip and expressed as the triangular load distribution as used in calculation step 2 of EBGEO.

The figure shows that the measured A agrees well with the A calculated with the concentric arches model. It can therefore be concluded that the total measured $B + C$ per pile also agrees well with the calculated $B + C$, as $B + C$ = total load − A. The figure also shows clearly that the concentric arches model concentrates the load on the GR strips. And the load on the GR strips is concentrated near the pile cap in a way resembling the inverse triangular load distribution. The concentric arches obviously explain the observed concentration of load near the pile caps. The concentric model agrees better with the observed load distribution than any of the other available analytical models.

5.5. Ground pressure versus depth

Fig. 20 compares the measured ground pressure (Zaeske, 2001) with the results of the concentric arches model, EBGEO, and Hewlett and Randolph (1988). The figure shows that the concentric arches model over-predicts the fall in ground pressure with depth, but that it is the only model that more or less follows the measured tendency of falling pressures with depth.

5.6. Parameter study

Fig. 21a shows that an increasing friction angle φ gives increasing arching. The figure shows the measured results for tests T2 and T3. These tests are the same, except for the embankment fill, as indicated in the figure and in Table 1. The figure shows that the concentric arches model is a better fit for the measurements than the others. The influence of φ is limited in the Hewlett and Randolph model for $\varphi > 30°$. Within this model of Hewlett and Randolph, the situation of one of two elements is normative: the crown

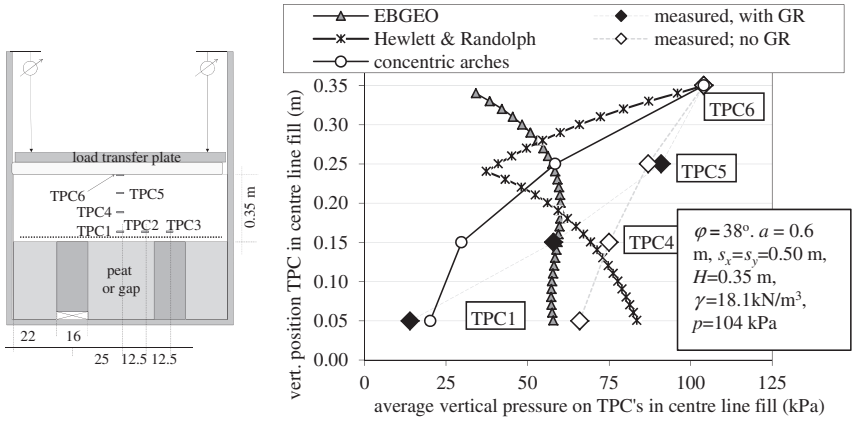

Fig. 20. Comparison of analytical calculations with measurements in Zaeske (2001, p. 63). For comparison reasons, measurements for the situation with and without GR are given (2001, p. 55 and 63), see also Fig. 6.

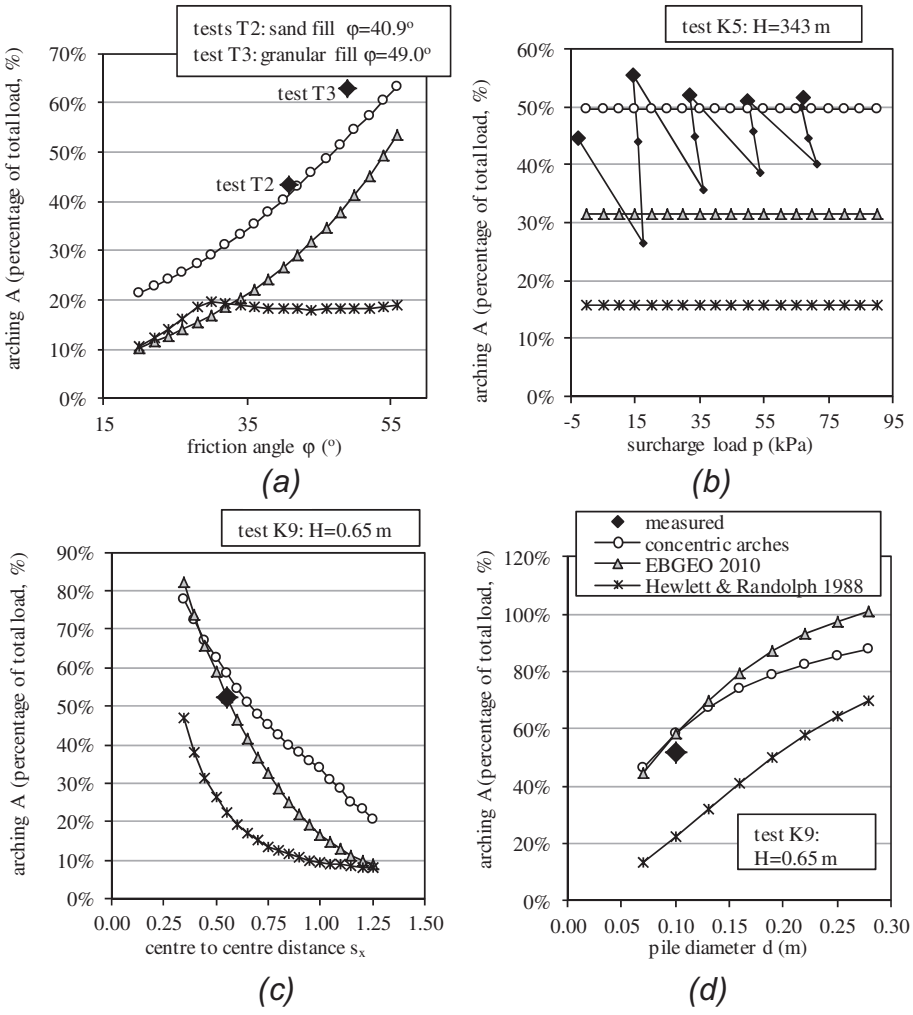

Fig. 21. Comparison of calculations and measurements in tests T2, T3, K5 and K9. See Table 1 for test specifications. Parameter study: variation of (a) friction angle φ, (b) surcharge load p. The large dots show the situation with a minimum of subsoil support measured just before a surcharge load increase, (c) centre-to-centre distance $s_x = s_y$ and (d) pile diameter d.

element or the foot element as indicated in Fig. 2. For $\varphi < 30°$, the foot element is normative, for $\varphi > 30°$, the crown element is normative. For the crown element, the pressure on the subsurface consists of two terms: the radial stress immediately below the arch, σ_i, and the soil weight below the arch. For $\varphi > 30°$, σ_i is so small that the soil weight below the arch dominates. Soil weight is independent of φ and therefore constant.

A% in all three models considered is independent of the surcharge load. This is because the models first calculate the load distribution for the situation without surcharge load ($p = 0$ kPa) and then multiply the result by the factor $(\gamma H + p)/(\gamma H)$. This is shown in Fig. 21b. This figure compares the measurements and calculations for test K5. The large dots are the measurements for the situations with a minimum of subsoil support. The figure shows that the measured A%, for the situation with a minimum of subsoil support, is indeed more or less constant: the large dots, especially with the higher surcharges, are located more or less on a horizontal line.

Fig. 21c and d show variation in the geometric properties; the centre-to-centre distance s_x of the piles and the pile diameter d. It is not possible to compare this with the measurements because these features were not varied in the tests. The tendency in the figures confirms expectations: larger pile spacing gives less arching; larger pile cap diameter gives more arching.

6. Conclusions

In model tests, numerical studies and field measurements of geosynthetic reinforced piled embankments, the following features were observed:

There is a major difference between piled embankments with or without GR. GR makes arching much more efficient: the load is transferred to the piles much more efficiently. With GR, the load on the GR is concentrated on the GR strips and can be described approximately as an inverse triangular load distribution on the GR strips. The difference between piled embankments with or without GR requires a distinction between models describing one or the other situation.

The observed load distribution in the piled embankments with GR is neither described nor explained by any of the available analytical models.

EBGEO tends to under-predict arching, although prediction accuracy is acceptable in one of the field tests considered. Arching A% increases with embankment height and seems to stabilise for the higher embankments. Consolidation of the subsoil results in an increase in arching (increasing arching A). This is different from results obtained using most of the available calculation models. A higher friction angle of the fill gives more arching, especially during subsoil consolidation.

A new equilibrium model was presented in this paper: the concentric arches model. It is a variation on the Hewlett and Randolph (1988) and EBGEO (Zaeske, 2001) equilibrium models. The model consists of a set of concentric hemispheres and arches. Larger hemispheres or arches exert more pressure on their subsurface.

A set of concentric 3D hemispheres transfer their load to a set of 2D arches between adjacent piles. These 2D arches transfer their load further to the piles. The model results in a load distribution on the GR that resembles the load distribution observed in experiments, field measurements and numerical analysis: the load is mainly concentrated on the GR strips with an approximately inverse triangular load distribution.

The model therefore provides a satisfactory physical explanation for this observed load distribution. The concentric stress arches were also found by several authors presenting numerical studies on arching such as Vermeer et al. (2001), Nadukuru and Michalowski (2012) and Han et al. (2012).

The concentric arches model explains increasing arching with subsoil consolidation (GR deflection). The explanation is that new arches are formed in succession as GR deflection progresses. However, in the limit-state version of the model presented in this paper, the model behaves in a rigid-plastic way and no longer describes the influence of subsoil consolidation or deformation.

The new model describes both full and partial arching, the latter with a relatively thin embankment.

Agreement between measured arching A and calculations made with the concentric arches model is good, and generally better than the EBGEO/CUR results, especially for relatively thin embankments. This finding is important for design calculations for the construction phase.

The concentric arches model is dependent on the embankment height and the fill friction angle φ in a way similar to that found in the experiments and in the numerical calculations of Le Hello and Villard (2009).

Ground pressure in the embankment decreases with depth and the tendency for decreasing pressure is similar in the Zaeske measurements (2001) and the concentric arches model. Furthermore, this model matches Zaeske's observations better than any of the other models considered.

Parameter variation indicates that the response of the concentric arches model to variations of surcharge load and geometry is reasonable.

Acknowledgements

The financial support from Deltares and the manufacturers Naue, TenCate and Huesker for the research was greatly appreciated. The test series was carried out as a result of close cooperation between Deltares and the suppliers TenCate, Huesker, Naue and Tensar. Their financial support and fruitful debate have been extremely valuable. The authors are grateful for the useful comments of the reviewers.

Appendix A. Derivation of the equations of the concentric arches model

A.1. The 2D arch: radial equilibrium

Consider Fig. 12. The areas and volume of the crown element are (neglecting terms with a product of more than one increment):

$$\begin{aligned}&\text{area below}: \mathrm{d}A_i = r\cdot\delta\theta\\ &\text{top area}: \mathrm{d}A_o = (r+\mathrm{d}r)\cdot\delta\theta = r\cdot\delta\theta+\mathrm{d}r\cdot\delta\theta\\ &\text{side area}: \mathrm{d}A_s = \mathrm{d}r\\ &\text{volume crown element}: \mathrm{d}V\approx r\cdot\delta\theta\cdot\mathrm{d}r\end{aligned} \tag{17}$$

For this 2D plane strain situation, these properties (areas and volume) apply for a unit length in the third dimension. For example $\mathrm{d}A_i = r\cdot\delta\theta\cdot 1$, where the '1' is 1 m. The areas $\mathrm{d}A_i$, dA_o and $\mathrm{d}A_s$ are therefore expressed in m^2, and $\mathrm{d}V$ in m^3. From the vertical (radial) equilibrium of the crown element, it follows that:

$$-\sigma_r\cdot\mathrm{d}A_i+(\sigma_r+\mathrm{d}\sigma_r)\cdot\mathrm{d}A_0-2\cdot\sigma_\theta\cdot\mathrm{d}A_s\cdot\sin\left(\frac{\delta\theta}{2}\right)+\gamma\cdot\mathrm{d}V=0 \tag{18}$$

The stresses σ_r and σ_θ are expressed in kPa and γ in kN/m^3. From substituting equations (17), and assuming that $\sin(\delta\theta)\approx\delta\theta$, it follows that:

$$-\sigma_r\cdot r\cdot\delta\theta+(\sigma_r+\mathrm{d}\sigma_r)\cdot(r\cdot\delta\theta+\mathrm{d}r\cdot\delta\theta)-2\cdot\sigma_\theta\cdot\mathrm{d}r\cdot\left(\frac{\delta\theta}{2}\right)+\gamma\cdot r\cdot\delta\theta\cdot\mathrm{d}r=0 \tag{19}$$

$$\frac{\mathrm{d}\sigma_r}{\mathrm{d}r}+\frac{\mathrm{d}\sigma_r}{r}+\frac{\sigma_r-\sigma_\theta}{r}+\gamma=0 \tag{20}$$

where σ_r is expressed in kPa. From $(\mathrm{d}\sigma_r/r)\to 0$, it follows that:

$$\frac{\mathrm{d}\sigma_r}{\mathrm{d}r}+\frac{(\sigma_r-\sigma_\theta)}{r}=-\gamma \tag{21}$$

We assume that the stress state in the arch is uniform around the semi-circle and that the limit state occurs in the entire arch.

$$\sigma_\theta = K_p\cdot\sigma_r = \frac{1+\sin\varphi}{1-\sin\varphi}\cdot\sigma_r \tag{22}$$

This results in the 2D differential equation for the radial stress in 2D arches:

$$\frac{\mathrm{d}\sigma_r}{\mathrm{d}r}+\frac{(1-K_p)}{r}\cdot\sigma_r=-\gamma \tag{23}$$

To solve this differential equation, it can be rewritten as

$$\frac{\mathrm{d}\sigma_r}{\mathrm{d}r}+p(r)\cdot\sigma_r=q(r) \tag{24}$$

where

$$p(r)=\frac{(1-K_p)}{r}\quad\text{and}\quad q(r)=-\gamma \tag{25}$$

The left-hand and right-hand sides of Eq. (23) are multiplied by an integration factor: $e^{\int p(r)\mathrm{d}r}$. This standard procedure to solve this kind of differential equation results in:

$$\frac{\mathrm{d}}{\mathrm{d}r}\left(e^{\int p(r)\mathrm{d}r}\cdot\sigma_R\right)=e^{\int p(r)\mathrm{d}r}q(r) \tag{26}$$

We find:

$$e^{\int p(r)\mathrm{d}r} = e^{\int \frac{1-K_p}{r}\mathrm{d}r} = e^{(1-K_p)\ln r} = r^{1-K_p} \tag{27}$$

Thus Eq. (26) becomes:

$$\frac{\mathrm{d}}{\mathrm{d}r}\left(r^{1-K_p}\cdot\sigma_r\right) = q(r)\cdot r^{1-K_p} = -\gamma\cdot r^{1-K_p} \tag{28}$$

$$\rightarrow r^{1-K_p}\cdot\sigma_r = -\gamma\int r^{1-K_p}\mathrm{d}r = -\frac{\gamma}{2-K_p}\cdot r^{2-K_p} + C \tag{29}$$

where C is a constant. Thus

$$\sigma_r = -\frac{\gamma}{2-K_p}\cdot\frac{r^{2-K_p}}{r^{1-K_p}} + \frac{C}{r^{1-K_p}} \tag{30}$$

thus

$$\sigma_r = C\cdot r^{K_p-1} + \frac{\gamma}{K_p-2}\cdot r \tag{31}$$

For the weightless case we find equation (3) of Hewlett and Randolph's (1988):

$$\sigma_r = C\cdot r^{K_p-1} \tag{32}$$

The boundary condition on the outside of the 2D arch is:

$$r = H_{g2D} \rightarrow \sigma_r = \gamma(H - H_{g2D}) + p \tag{33}$$

where H_{g2D} is the height of the largest 2D arch and given by Eq. (2). Substitution of this condition into Eq. (31) gives:

$$\begin{aligned} &C\cdot\left(H_{g2D}\right)^{(K_p-1)} + \frac{\gamma}{K_p-2}\cdot H_{g2D} = \gamma(H - H_{g2D}) + p \\ &\rightarrow C = H_{g2D}^{(1-K_p)}\cdot\left[\gamma H + p - \gamma H_{g2D}\frac{(K_p-1)}{(K_p-2)}\right] \end{aligned} \tag{34}$$

thus

$$\rightarrow \sigma_r = \left(\frac{2}{s_x}\right)^{(K_p-1)}\cdot\left[\gamma H + p - \frac{s_x\gamma}{2}\frac{(K_p-1)}{(K_p-2)}\right]\cdot r^{(K_p-1)} + \frac{\gamma}{K_p-2}\cdot r \tag{35}$$

As the tangential stress $\sigma_\theta = K_p\cdot\sigma_r$ in kPa, we find:

$$\sigma_\theta = P_{2D}\cdot r^{(K_p-1)} + Q_{2D}\cdot r \tag{36}$$

where we have defined P_{2D} and Q_{2D} as:

$$P_{2D} = K_p\cdot\left(\frac{2}{s_x}\right)^{(K_p-1)}\cdot\left[\gamma H + p - \frac{s_x\gamma}{2}\frac{(K_p-1)}{(K_p-2)}\right] \text{ and}$$
$$Q_{2D} = K_p\cdot\frac{\gamma}{K_p-2}$$

A.2. The 3D arch: radial equilibrium

Consider Fig. 13. The areas and volume of the crown element are (neglecting terms with a product of more than one increment):

$$\begin{aligned} &\text{area below}: \mathrm{d}A_i = \frac{1}{4}\pi\cdot(R\cdot\delta\theta)^2 = \frac{1}{4}\pi\cdot R^2\cdot\delta\theta^2 \\ &\text{top area}: \mathrm{d}A_o = \frac{1}{4}\pi\cdot(R+\mathrm{d}R)^2\cdot\delta\theta^2 \approx \frac{1}{4}\pi\cdot\left(R^2\cdot\delta\theta^2 + 2R\cdot\mathrm{d}R\cdot\delta\theta^2\right) \\ &\text{side area}: \mathrm{d}A_s \approx \pi\cdot R\cdot\delta\theta\cdot\mathrm{d}R \\ &\text{volume crown element}: \mathrm{d}V \approx \frac{1}{4}\pi\cdot R^2\cdot\delta\theta^2\cdot\mathrm{d}R \end{aligned} \tag{37}$$

From the vertical (radial) equilibrium of the crown element, it follows that:

$$-\sigma_R\cdot\mathrm{d}A_i + (\sigma_R + \mathrm{d}\sigma_R)\cdot\mathrm{d}A_0 - \sigma_\theta\cdot\sin\left(\frac{\delta\theta}{2}\right)\cdot\mathrm{d}A_s + \gamma\cdot\mathrm{d}V = 0 \tag{38}$$

From substituting equations (37), and assuming $\sin(\delta\theta) \approx \delta\theta$, it follows that:

$$\begin{aligned} &-\sigma_R\cdot\frac{1}{4}\pi\cdot R^2\cdot\delta\theta^2 + (\sigma_R + \mathrm{d}\sigma_R)\cdot\frac{1}{4}\pi\cdot\left(R^2\cdot\delta\theta^2 + 2R\cdot\mathrm{d}R\cdot\delta\theta^2\right) \\ &-\sigma_\theta\cdot\left(\frac{\delta\theta}{2}\right)\cdot\pi\cdot R\cdot\delta\theta\cdot\mathrm{d}R + \gamma\cdot\frac{1}{4}\pi\cdot R^2\cdot\delta\theta^2\cdot\mathrm{d}R = 0 \end{aligned} \tag{39}$$

From neglecting terms with a product of more than one increment, it follows that:

$$\frac{\mathrm{d}\sigma_R}{\mathrm{d}R} + \frac{2(\sigma_R - \sigma_\theta)}{R} + \gamma = 0 \tag{40}$$

In the weightless case, the stress state in the arch is uniform around the semi-circle. It is assumed that the limit state occurs in the entire arch.

$$\sigma_\theta = K_p\cdot\sigma_R = \frac{1+\sin\varphi}{1-\sin\varphi}\cdot\sigma_R \tag{41}$$

This results in:

$$\frac{\mathrm{d}\sigma_R}{\mathrm{d}R} + \frac{2(1-K_p)}{R}\cdot\sigma_R = -\gamma \tag{42}$$

which is the differential equation for the radial stress in the 3D hemisphere. So far, the explanation is the same as Hewlett and Randolph's (1988). To solve this differential equation, Eq. (23) can be rewritten as:

$$\frac{\mathrm{d}}{\mathrm{d}R}\left(e^{\int p(R)\mathrm{d}R}\cdot\sigma_R\right) = e^{\int p(R)\mathrm{d}R}q(R) \tag{43}$$

with:

$$\begin{aligned} &p(R) = \frac{2(1-K_p)}{R} = \frac{\alpha}{R} \text{ and } q(R) = -\gamma \\ &\text{and } \alpha = 2(1-K_p) \end{aligned} \tag{44}$$

We find:

$$e^{\int p(R)\mathrm{d}R} = e^{\int \frac{\alpha}{R}\mathrm{d}R} = e^{\alpha\ln R} = R^\alpha \tag{45}$$

Thus Eq. (43) becomes:

$$\frac{\mathrm{d}}{\mathrm{d}R}(R^{\alpha}\cdot\sigma_R) = q(R)\cdot R^{\alpha} = -\gamma\cdot R^{\alpha} \tag{46}$$

$$\rightarrow R^{\alpha}\cdot\sigma_R = -\frac{\gamma}{\alpha+1}\cdot R^{\alpha+1} + C \tag{47}$$

where C is a constant. Thus

$$\begin{aligned}\sigma_R &= -\frac{\gamma}{\alpha+1}\cdot R + \frac{C}{R^{\alpha}}\\ \rightarrow\sigma_R &= C\cdot R^{2(K_p-1)} + \frac{\gamma}{2K_p-3}\cdot R\end{aligned} \tag{48}$$

The outer radius of the hemisphere is $R_o = s_x/\sqrt{2}$. The surcharge load will first be neglected and taken into account afterwards, analogous to Zaeske (2001) and Hewlett and Randolph (1988). The boundary condition on the outside of the arch is:

$$R = R_o = H_{g3D} \rightarrow \sigma_R = \gamma(H - H_{g3D}) \tag{49}$$

where the arch height H_{g3D} is given by Eq. (4). Substitution of this condition into Eq. (48) gives:

$$\begin{aligned}C\cdot H_{g3D}^{2(K_p-1)} + \frac{\gamma}{2K_p-3}\cdot H_{g3D} &= \gamma(H - H_{g3D})\\ \rightarrow C &= \gamma\cdot H_{g3D}^{2-2K_p}\cdot\left[H - H_{g3D}\cdot\left(\frac{2K_p-2}{2K_p-3}\right)\right]\end{aligned} \tag{50}$$

thus

$$\rightarrow\sigma_R = \gamma\cdot H_{g3D}^{2-2K_p}\cdot\left[H - H_{g3D}\cdot\left(\frac{2K_p-2}{2K_p-3}\right)\right]\cdot R^{2K_p-2} + \frac{\gamma}{2K_p-3}\cdot R \tag{51}$$

As $\sigma_\theta = K_p\,\sigma_r$, we find:

$$\sigma_\theta = P_{3D}\cdot R^{2K_p-2} + Q_{3D}\cdot R \tag{52}$$

where we have defined P_{3D} and Q_{3D} as:

$$P_{3D} = \gamma\cdot K_p\cdot H_{g3D}^{2-2K_p}\cdot\left[H - H_{g3D}\cdot\left(\frac{2K_p-2}{2K_p-3}\right)\right] \text{ and}$$

$$Q_{3D} = K_p\cdot\frac{\gamma}{2K_p-3}$$

So far, Hewlett and Randolph used the same explanation. However, a difference is that they limit the height of their arch to half the width of the pile cap, while the equation of the concentric arches model is extended downwards to the subsurface where $R = 0$. Hewlett and Randolph (1988) therefore use Eq. (52) for $R_i < R < R_o$, and we use the equation for $0 < R < R_o$, where for full arching: $R_o = H_{g3D} = 0.5s_d$ and $R_i = 0.5(s_d - d)$.

A.3. Derivation of load exerted on GR

Arching is assumed to transfer the load in two steps. The first step is that the load is transferred in the direction of the ring of GR strips and pile caps. This is done along the 3D hemispheres. The second step is that the load is transferred further in the direction of the pile caps along the 2D arches between each two adjacent pile caps. The 2D and 3D arches exert a total force on the subsurface. The total force exerted on the GR ($B + C$ in kN/pile) may be obtained by integrating the tangential stress σ_θ across the area of the GR. The general equation is:

$$B + C = F_{GR} = \int_{GRarea} \sigma_\theta \mathrm{d}A_{GR} \tag{53}$$

The total load $B + C$ on the subsurface, F_{GR}, consists of two parts along the two arching steps described above: $F_{GRsquare}$ and $F_{GRstrips}$:

1. 3D hemispheres transfer the load in the direction of the ring of GR strips and pile caps. The 3D hemispheres exert a vertical load on their GRsquare (indicated in Fig. 11). This is the first load part, $F_{GRsquare}$, of the load on the subsurface.
2. The 2D arches above the GR strips transfer the load further in the direction of the pile caps. The 2D arches exert a vertical load on the GR strips. This is the second load part, $F_{GRstrips}$, of the load on the subsurface.

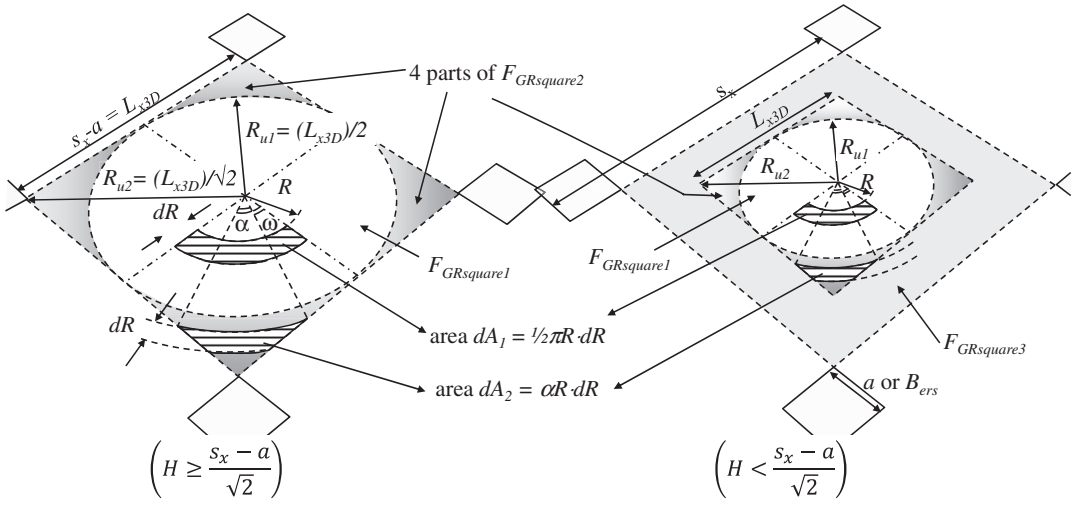

Fig. 22. Integrating the tangential stress σ_θ across the square area where the 3D hemispheres exert their load.

Total force on the GR square; determination of $F_{GRsquare}$

Consider Fig. 22. As long as $H \geq ((s_x - a)/\sqrt{2})$, $F_{GRsquare}$ consists of the load exerted by the hemispheres only. In that case (on the left of Fig. 22), the total force exerted on the GRsquare may be obtained by integrating the tangential stress σ_θ in the 3D hemispheres across the GRsquare. When $H < ((s_x - a)/\sqrt{2})$, the total force exerted on the GRsquare may be obtained by integrating the tangential stress σ_θ across the smaller ($L_{x3D}\cdot L_{x3D}$-)square, with width L_{x3D}, as indicated on the right of Fig. 22. The load F_{GRsq3} on the area outside this $L_{x3D}\cdot L_{x3D}$-square and inside the GRsquare is assumed to be $\gamma H + p$, which will be derived for later on. L_{x3D} is defined as follows:

$$\begin{aligned} L_{x3D} &= s_x - a \qquad \text{for } H \geq \frac{s_x - a}{\sqrt{2}} \\ L_{x3D} &= \sqrt{2}\cdot H_{g3D} \quad \text{for } H < \frac{s_x - a}{\sqrt{2}} \end{aligned} \tag{54}$$

where H_{g3D} in defined in Eq. (4).

For the situation in which $s_x \neq s_y$ the integration is carried out for an imaginary square with width L_{x3D}. This width is determined as:

$$\begin{aligned} L_{3D} &= \tfrac{1}{\sqrt{2}}\sqrt{(s_x-a)^2+(s_y-a)^2} \quad \text{for } H \geq \tfrac{1}{2}\sqrt{(s_x-a)^2+(s_y-a)^2} \\ L_{3D} &= \sqrt{2}\cdot H_{g3D} \qquad\qquad\qquad\quad \text{for } H < \tfrac{1}{2}\sqrt{(s_x-a)^2+(s_y-a)^2} \end{aligned} \tag{55}$$

Considering the situation that $H \geq (1/2)\sqrt{(s_x-a)^2+(s_y-a)^2}$, the square with width L_{3D} has the same diagonal as the area between the four piles. Integrating the tangential stress across this imaginary square gives the same or a higher force on the GR square than numerical integration of the tangential stress over the rectangular between the four piles. In the remainder of this appendix, the situation with $s_x = s_y$ applies.

The total force $F_{GRsquare}$ on the GR square is derived by dividing the square into three sections:

- part $F_{GRsquare1}$, inside the largest circle in the $L_{x3D}\cdot L_{x3D}$-square (white in Fig. 22).
- part $F_{GRsquare2}$, outside the circle but inside the $L_{x3D}\cdot L_{x3D}$-square (dark grey Fig. 22).
- part $F_{GRsquare3}$, outside the $L_{x3D}\cdot L_{x3D}$-square but inside the GR square (light grey in the right-hand figure in Fig. 22).

The three terms are calculated with surcharge load $p = 0$, and will afterwards be multiplied by the term $(\gamma H + p)/\gamma H$ to find the total load on the GR square:

$$\begin{aligned} F_{GRsquare} &= F_{GRsquare1} + F_{GRsquare2} + F_{GRsquare3} \\ &= \left(\frac{\gamma H + p}{\gamma H}\right)\cdot\left(F_{GRsq1p=0} + F_{GRsq2p=0} + F_{GRsq3p=0}\right) \end{aligned} \tag{56}$$

The first load part, $F_{GRsquare1}$, which rests on the circular area in the largest circle, is determined as follows:

$$\begin{aligned} F_{GRsq1p=0} &= 4\int_0^{R_{u1}} \sigma_\theta \mathrm{d}A_{GR} = 4\int_0^{R_{u1}} \sigma_\theta \frac{1}{2}\pi R\,\mathrm{d}R \\ &= 2\pi\int_0^{R_{u1}} \left(P_{3D}\cdot(R)^{2K_p-1} + Q_{3D}\cdot R^2\right)\mathrm{d}R \\ F_{GRsq1p=0} &= 2\pi\left[\frac{P_{3D}}{2K_p}\cdot(R)^{2K_p} + \frac{1}{3}Q_{3D}\cdot R^3\right]_0^{R_{u1}=\frac{L_{x3D}}{2}} \\ F_{GRsquare1} &= \left(1+\frac{p}{\gamma H}\right)\cdot\left(\frac{\pi P_{3D}}{K_p}\cdot\left(\frac{L_{x3D}}{2}\right)^{2K_p} + \frac{2}{3}\pi Q_{3D}\cdot\left(\frac{L_{x3D}}{2}\right)^3\right) \end{aligned} \tag{57}$$

where σ_θ, P_{3D} and Q_{3D} are given in Eq. (52). The second load part, $F_{GRsquare2}$, which rests on the area within the square but outside the circle, is dependent on angle α. This angle α is a function of R, and can be read from Fig. 22, as the complementary angle $\omega = \arccos\left(\frac{R_{u1}}{R}\right) = \arccos\left(\frac{L_{x3D}}{2R}\right)$. We therefore find, for α:

$$\alpha = \frac{\pi}{2} - 2\arccos\left(\frac{L_{x3D}}{2R}\right) \tag{58}$$

The force on the grey areas in Fig. 22 (outside the circle, inside the GR square) should therefore be determined by:

$$F_{GRsquare2} = \left(1+\tfrac{p}{\gamma H}\right)\cdot F_{GRsq2p=0}$$

where

$$\begin{aligned} F_{GRsq2p=0} &= 4\int_{R_{u1}}^{R_{u2}} \sigma_\theta \mathrm{d}A_{GRsq2} = 4\int_{R_{u1}}^{R_{u2}} \sigma_\theta \alpha R\,\mathrm{d}R \\ &= 4\int_{R_{u1}}^{R_{u2}} \left(P_{3D}\cdot(R)^{2K_p-2} + Q_{3D}\cdot R\right)\alpha R\,\mathrm{d}R \\ \rightarrow F_{GRsq2p=0} &= 4\int_{R_{u1}}^{R_{u2}} \left(P_{3D}\cdot(R)^{2K_p-2} + Q_{3D}\cdot R\right) \\ &\times\left(\frac{\pi}{2} - 2\arccos\left(\frac{L_{x3D}}{2R}\right)\right)R\,\mathrm{d}R \end{aligned} \tag{59}$$

This integral can be separated into four terms, which will be solved separately:

$$F_{GRsq2p=0} = {}_1F_{GRsq2} + {}_2F_{GRsq2} + {}_3F_{GRsq2} + {}_4F_{GRsq2}$$

where

$$
\begin{aligned}
{}_1F_{\mathrm{GRsq2}} &= 2\pi P_{3\mathrm{D}} \int_{R_{u1}}^{R_{u2}} R^{2K_p-1}\mathrm{d}R \\
{}_2F_{\mathrm{GRsq2}} &= 2\pi Q_{3\mathrm{D}} \int_{R_{u1}}^{R_{u2}} R^{2}\mathrm{d}R \\
{}_3F_{\mathrm{GRsq2}} &= -8P_{3\mathrm{D}} \int_{R_{u1}}^{R_{u2}} R^{2K_p-1}\arccos\left(\frac{L_{x3\mathrm{D}}}{2R}\right)\mathrm{d}R \\
{}_4F_{\mathrm{GRsq2}} &= -8Q_{3\mathrm{D}} \int_{R_{u1}}^{R_{u2}} R^{2}\arccos\left(\frac{L_{x3\mathrm{D}}}{2R}\right)\mathrm{d}R
\end{aligned}
\tag{60}
$$

The first two terms are solved as follows (R_{u2} and R_{u1} are indicated in Fig. 22):

$$
\begin{aligned}
{}_1F_{\mathrm{GRsq2}} &= \frac{2\pi P_{3\mathrm{D}}}{2K_p}R^{2K_p}\Big|_{R_{u1}}^{R_{u2}} = \frac{\pi P_{3\mathrm{D}}}{K_p}\left(2^{K_p}-1\right)\left(\frac{L_{x3\mathrm{D}}}{2}\right)^{2K_p} \\
{}_2F_{\mathrm{GRsq2}} &= \frac{2\pi Q_{3\mathrm{D}}}{3}R^{3}\Big|_{R_{u1}}^{R_{u2}} = \frac{2\pi Q_{3\mathrm{D}}}{3}\left(\left(\sqrt{2}\right)^3-1\right)\left(\frac{L_{x3\mathrm{D}}}{2}\right)^{3}
\end{aligned}
\tag{61}
$$

The other two integral terms are re-written as:

$$
\begin{aligned}
-\frac{{}^3F_{\mathrm{GRsq2}}}{8P_{3\mathrm{D}}} &= \int_{R_{u1}}^{R_{u2}} R^{2K_p-1}\arccos\left(\frac{L_{x3\mathrm{D}}}{2R}\right)\mathrm{d}R \\
-\frac{{}^4F_{\mathrm{GRsq2}}}{8Q_{3\mathrm{D}}} &= \int_{R_{u1}}^{R_{u2}} R^{2}\arccos\left(\frac{L_{x3\mathrm{D}}}{2R}\right)\mathrm{d}R
\end{aligned}
\tag{62}
$$

We continue with solving the fourth term, ${}_4F_{\mathrm{GRsq2}}$, and substitute:

$$
\begin{gathered}
\rho = \frac{L_{x3\mathrm{D}}}{2R} \text{ thus } R = \frac{L_{x3\mathrm{D}}}{2\rho} \text{ and } \mathrm{d}R = -\frac{L_{x3\mathrm{D}}}{2\rho^2}\mathrm{d}\rho \\
\rightarrow \int_{R_{u1}=\frac{L_{x3\mathrm{D}}}{2}}^{R_{u2}=\frac{L_{x3\mathrm{D}}}{\sqrt{2}}} \mathrm{d}R = \int_{\frac{L_{x3\mathrm{D}}}{2R_{u1}}=\frac{L_{x3\mathrm{D}}}{2\cdot\frac{L_{x3\mathrm{D}}}{2}}=1}^{\frac{L_{x3\mathrm{D}}}{2R_{u2}}=\frac{L_{x3\mathrm{D}}}{2\cdot\frac{L_{x3\mathrm{D}}}{\sqrt{2}}}=\frac{1}{2}\sqrt{2}} \mathrm{d}\rho
\end{gathered}
\tag{63}
$$

where ρ is the cosine of the complementary angle $\omega = \arccos\left(\frac{L_{x3\mathrm{D}}}{2R}\right)$ in Fig. 22. Thus

$$
\begin{aligned}
\frac{{}^4F_{\mathrm{GRsq2}}}{8Q_{3\mathrm{D}}} &= \int_{1}^{\frac{1}{2}\sqrt{2}} \left(\frac{L_{x3\mathrm{D}}}{2\rho}\right)^2 \arccos\rho\left(\frac{L_{x3\mathrm{D}}}{2\rho^2}\right)\mathrm{d}\rho \\
\rightarrow \frac{{}^4F_{\mathrm{GRsq2}}}{Q_{3\mathrm{D}}(L_{x3\mathrm{D}})^3} &= \int_{1}^{\frac{1}{2}\sqrt{2}} \rho^{-4}\arccos\rho\mathrm{d}\rho
\end{aligned}
\tag{64}
$$

We bring the power to the increment

$$
-\frac{3\cdot{}_4F_{\mathrm{GRsq2}}}{Q_{3\mathrm{D}}(L_{x3\mathrm{D}})^3} = \int_{1}^{\frac{1}{2}\sqrt{2}} \arccos\rho\mathrm{d}\left(\rho^{-3}\right) \tag{65}
$$

Partial integration gives:

$$
-\frac{3\cdot{}_4F_{\mathrm{GRsq2}}}{Q_{3\mathrm{D}}(L_{x3\mathrm{D}})^3} = \rho^{-3}\arccos\rho\Big|_{1}^{\frac{1}{2}\sqrt{2}} - \int_{1}^{\frac{1}{2}\sqrt{2}} \rho^{-3}d(\arccos\rho) \tag{66}
$$

As $(\mathrm{d}/\mathrm{d}\rho)(\arccos\rho) = -\frac{1}{\sqrt{1-\rho^2}}$, we find:

$$
-\frac{3\cdot{}_4F_{\mathrm{GRsq2}}}{Q_{3\mathrm{D}}(L_{x3\mathrm{D}})^3} = \frac{\pi}{\sqrt{2}} + \int_{1}^{\frac{1}{2}\sqrt{2}} \frac{\rho^{-3}}{\sqrt{1-\rho^2}}\mathrm{d}\rho \tag{67}
$$

We substitute:

$$
\begin{gathered}
\frac{1}{\sqrt{1-\rho^2}} = \frac{\sqrt{u^2+1}}{u} \\
\rightarrow \rho^{-2} = u^2+1 \\
\rightarrow -\rho^{-3}\mathrm{d}\rho = u\,\mathrm{d}u \\
\rightarrow \int_{\rho=1}^{\rho=\frac{1}{2}\sqrt{2}} \mathrm{d}\rho = \int_{u=\sqrt{\frac{1}{(1)^2}-1}=0}^{u=\sqrt{\frac{1}{\left(\frac{1}{2}\sqrt{2}\right)^2}-1}=1} \mathrm{d}u
\end{gathered}
\tag{68}
$$

This gives:

$$
-\frac{3\cdot{}_4F_{\mathrm{GRsq2}}}{Q_{3\mathrm{D}}(L_{x3\mathrm{D}})^3} = \frac{\pi}{\sqrt{2}} - \int_{0}^{1} \sqrt{u^2+1}\,\mathrm{d}u \tag{69}
$$

This gives, with any integral table:

$$
-\frac{3\cdot{}_4F_{\mathrm{GRsq2}}}{Q_{3\mathrm{D}}(L_{x3\mathrm{D}})^3} = \frac{\pi}{\sqrt{2}} - \frac{1}{2}\sqrt{2} - \frac{1}{2}\ln\left(1+\sqrt{2}\right) \tag{70}
$$

Thus

$$
{}_4F_{\mathrm{GRsq2}} = \frac{1}{6}Q_{3\mathrm{D}}(L_{x3\mathrm{D}})^3\cdot\left(\sqrt{2}(1-\pi)+\ln\left(1+\sqrt{2}\right)\right) \tag{71}
$$

The derivation of the third term, ${}_3F_{\mathrm{GRsq2}}$, follows the same procedure as for ${}_4F_{\mathrm{GRsq2}}$. With Eqs. (63) and (62) we find:

$$
\frac{{}_3F_{\mathrm{GRsq2}}\cdot 2^{2K_p-3}}{P_{3\mathrm{D}}\cdot(L_{x3\mathrm{D}})^{2K_p}} = \int_{1}^{\frac{1}{2}\sqrt{2}} \rho^{-2K_p-1}\arccos\rho\,\mathrm{d}\rho \tag{72}
$$

We bring the power to the increment:

$$\rho^{-2K_p-1} = \frac{1}{-2K_p}\mathrm{d}\rho^{-2K_p}$$
$$\rightarrow -\frac{2K_p\cdot {}_3F_{\mathrm{GRsq2}}\cdot 2^{2K_p-3}}{P_{3\mathrm{D}}\cdot(L_{x3\mathrm{D}})^{2K_p}} = \int_1^{\frac{1}{2}\sqrt{2}} \arccos\rho\,\mathrm{d}\rho^{-2K_p} \tag{73}$$

Partial integration:

$$-\frac{K_p\cdot {}_3F_{\mathrm{GRsq2}}\cdot 2^{2K_p-2}}{P_{3\mathrm{D}}\cdot(L_{x3\mathrm{D}})^{2K_p}} = \rho^{-2K_p}\arccos\rho\Big|_1^{\frac{1}{2}\sqrt{2}} - \int_1^{\frac{1}{2}\sqrt{2}} \rho^{-2K_p}\mathrm{d}(\arccos\rho) \tag{74}$$

thus

$$-\frac{K_p\cdot {}_3F_{\mathrm{GRsq2}}\cdot 2^{2K_p-2}}{P_{3\mathrm{D}}\cdot(L_{x3\mathrm{D}})^{2K_p}} = \frac{\pi}{2^{2-K_p}} - \int_1^{\frac{1}{2}\sqrt{2}} \frac{\rho^{-2K_p}}{\sqrt{1-\rho^2}}\mathrm{d}\rho \tag{75}$$

Finally, the substitution of:

$$\frac{1}{\sqrt{1-\rho^2}} = \frac{\sqrt{u^2+1}}{u}$$
$$\rightarrow \rho^{-2} = u^2+1 \rightarrow -\rho^{-3}\mathrm{d}\rho = u\,\mathrm{d}u$$
$$\rightarrow \rho^{-2K_p} = \left(u^2+1\right)^{K_p}$$
$$\rightarrow \rho^3 = \left(u^2+1\right)^{-\frac{3}{2}}$$
$$\rightarrow \mathrm{d}\rho = -u\rho^3\mathrm{d}u = -u\left(u^2+1\right)^{-\frac{3}{2}}\mathrm{d}u \tag{76}$$
$$\rho = \tfrac{1}{2}\sqrt{2} \qquad u = \sqrt{\frac{1}{\left(\frac{1}{2}\sqrt{2}\right)^2}-1} = 1$$
$$\rightarrow \int_{\rho=1} \mathrm{d}\rho = \int_{u=\sqrt{\frac{1}{(1)^2}-1}=0} \mathrm{d}u$$

gives:

$$-\frac{K_p\cdot {}_3F_{\mathrm{GRsq2}}\cdot 2^{2K_p-2}}{P_{3\mathrm{D}}\cdot(L_{x3\mathrm{D}})^{2K_p}} = \frac{\pi}{2^{2-K_p}} + \int_0^1 \frac{\sqrt{u^2+1}}{u}\left(u^2+1\right)^{K_p} u\left(u^2+1\right)^{-\frac{3}{2}}\mathrm{d}u$$
$$\rightarrow -\frac{K_p\cdot {}_3F_{\mathrm{GRsq2}}\cdot 2^{2K_p-2}}{P_{3\mathrm{D}}\cdot(L_{x3\mathrm{D}})^{2K_p}} = \frac{\pi}{2^{2-K_p}} + \int_0^1 \left(u^2+1\right)^{K_p-1}\mathrm{d}u \tag{77}$$

This last term can be rewritten with a binomial series:

$$\int_0^1 \left(u^2+1\right)^{K_p-1}\mathrm{d}u = \int_0^1 \sum_{n=0}^{\infty}\binom{K_p-1}{n} u^{2n}\mathrm{d}u \tag{78}$$

where

$$\sum_{n=0}^{\infty}\binom{K_p-1}{n}u^{2n} = 1 + (K_p-1)u^2 + \frac{(K_p-1)(K_p-2)}{2!}u^4 + \frac{(K_p-1)(K_p-2)(K_p-3)}{3!}u^6 + \cdots \tag{79}$$

From this, it follows that:

$$\int_0^1 \left(u^2+1\right)^{K_p-1}\mathrm{d}u = \frac{1}{2n+1}\sum_{n=0}^{\infty}\binom{K_p-1}{n}u^{2n+1}\Big|_0^1 = \sum_{n=0}^{\infty}\frac{1}{2n+1}\binom{K_p-1}{n} \tag{80}$$

$$\rightarrow -\frac{K_p\cdot {}_3F_{\mathrm{GRsq2}}\cdot 2^{2K_p-2}}{P_{3\mathrm{D}}\cdot(L_{x3\mathrm{D}})^{2K_p}} = \frac{\pi}{2^{2-K_p}} + \int_0^1 \left(u^2+1\right)^{K_p-1}\mathrm{d}u$$
$$-\frac{k_p\cdot {}_3F_{\mathrm{GRsq2}}\cdot 2^{2K_p-2}}{P_{3\mathrm{D}}\cdot(L_{x3\mathrm{D}})^{2K_p}} = \frac{\pi}{2^{2-K_p}} + \sum_{n=0}^{\infty}\frac{1}{2n+1}\binom{K_p-1}{n}$$
$$\rightarrow {}_3F_{\mathrm{GRsq2}} = -\frac{P_{3\mathrm{D}}\cdot 2^{2-2K_p}\cdot(L_{x3\mathrm{D}})^{2K_p}}{K_p}\cdot \times\left(\frac{\pi}{2^{2-K_p}} + \sum_{n=0}^{\infty}\frac{1}{2n+1}\binom{K_p-1}{n}\right)$$
$$= -\frac{P_{3\mathrm{D}}\cdot 2^{2-2K_p}\cdot(L_{x3\mathrm{D}})^{2K_p}}{K_p}\cdot\left(\frac{\pi}{2^{2-K_p}} + 1 + \frac{1}{3}(K_p-1)\right.$$
$$+\frac{1}{10}(K_p-1)(K_p-2) + \frac{1}{42}(K_p-1)(K_p-2)(K_p-3)$$
$$+\frac{1}{216}(K_p-1)(K_p-2)(K_p-3)(K_p-4)$$
$$+\frac{1}{1320}(K_p-1)(K_p-2)(K_p-3)(K_p-4)(K_p-5)$$
$$+\frac{1}{9360}(K_p-1)(K_p-2)(K_p-3)(K_p-4)(K_p-5)(K_p-6)$$
$$\left.+\cdots\cdots\right) \tag{81}$$

The resulting total load on the GR square for the case $s_x \neq s_y$ is given by Eq. (6) of this paper.

An alternative is to solve this numerically. This means that the GR square is divided into a large number of small areas. The average vertical stress on each increment is determined and multiplied by its area. The sum gives the total force on the GR square,

with F_{GRsquare} in kN/pile. $F_{\mathrm{GRsquare1}}$ and $F_{\mathrm{GRsquare2}}$ (kN/pile) are indicated in Fig. 22, where $H_{g3\mathrm{D}}$ (m) is the height of the largest hemisphere and $L_{x3\mathrm{D}}$ is the width of the square upon which the hemispheres exert a load, as indicated in Fig. 22. When $L_{x3\mathrm{D}} < (s_x - a)$, the area outside $L_{x3\mathrm{D}}$ but inside the GR square is assumed to be loaded by $\gamma H + p$. This gives an extra term, $F_{\mathrm{GRsq3}p=0}$, where

$$\begin{aligned} F_{\mathrm{GRsq3}p=0} &= \gamma H\cdot\left((s_x-a)^2 - L_{x3D}^2\right) && \text{for } L_{x3\mathrm{D}} < s_x - a \\ F_{\mathrm{GRsq3}p=0} &= 0 && \text{for } L_{x3\mathrm{D}} \geq s_x - a \end{aligned} \tag{82}$$

Note that it is assumed that $s_x = s_y$ in this appendix. In section 4.5 the equations are given for $s_x \neq s_y$. It is supposed that the load not resting on the GR square is transferred to the ring of GR strips and pile caps. This load is therefore applied as an equally

distributed surcharge load on the 2D arches. This surcharge load on the 2D arches is, in kN/pile:

$$F_{\text{transferred}} = \gamma H\cdot(s_x - a)^2 - \left(F_{\text{GRsq1}p=0} + F_{\text{GRsq2}p=0} + F_{\text{GRsq3}p=0}\right) \tag{83}$$

where a is the width of a square pile cap or the equivalent width of a circular pile cap. Distributed equally on the 2D arches, this results in a surcharge load in kPa (2 full GR strips and a pile cap per pile):

$$p_{\text{transferred}} = \frac{F_{\text{transferred}}}{2a\cdot(L_{x2D}) + a^2} \tag{84}$$

where

$$\begin{aligned} L_{x2D} &= s_x - a \quad \text{for } H \geq \tfrac{1}{2}(s_x - a) \\ L_{x2D} &= 2\cdot H_{g2D} \quad \text{for } H < \tfrac{1}{2}(s_x - a) \end{aligned} \tag{85}$$

where H_{g2D} in defined in Eq. (13).

Total force on the GR strip; determination of $F_{GRstrip}$

In this appendix, for reasons of clarity, it is assumed that $s_x = s_y$. The tangential stress σ_θ (kPa) in the 2D arches above the GR strips is now given by:

$$\sigma_\theta = P_{2D}\cdot r^{K_p-1} + Q_{2D}\cdot r$$

(2D arch), where

$$\begin{aligned} P_{2D} &= K_p\cdot H_{g2D}^{(1-K_p)}\cdot\left[\gamma H + p_{\text{transferred}} - \gamma H_{g2D}\cdot\left(\frac{K_p-1}{K_p-2}\right)\right] \\ Q_{2D} &= K_p\cdot\frac{\gamma}{K_p-2} \end{aligned} \tag{86}$$

where $p_{\text{transferred}}$ (kPa) is the load transferred from the 3D hemispheres to the 2D arches and given by Eq. (84) and H_{g2D} (m) is the height of the 2D arch and given by Eq. (13). When $s_x \neq s_y$, a distinction should be made between P_{x2D} versus P_{y2D} and H_{xg2D} versus H_{yg2D}. The rest of the equation is equal to Eq. (1) in this paper. The total force on the GR strip (without surcharge load p) may be obtained by integrating the tangential stress σ_θ across the area of the GR strip as shown in Fig. 23. The total force on two GR strips (in kN/pile) is therefore:

$$\begin{aligned} F_{GRstrip} &= F_{GRstrip\ 1} + F_{GRstrip\ 2} \\ &= \left(\frac{\gamma H + p}{\gamma H}\right)\cdot\left(F_{GRstr\ 1\ p=0} + F_{GRstr\ 2\ p=0}\right) \end{aligned} \tag{87}$$

where

$$\begin{aligned} F_{\text{GRstr1}p=0} &= 4\int_0^{r_0}\sigma_\theta \mathrm{d}A_{\text{GRstrip}} = 4\int_0^{r_0}\sigma_\theta\cdot a\,\mathrm{d}r \\ &= 4a\int_0^{\frac{1}{2}L_{x2D}}\left(P_{2D}\cdot r^{(K_p-1)} + Q_{2D}\cdot r\right)\mathrm{d}r \end{aligned} \tag{88}$$

thus

$$\begin{aligned} F_{\text{GRstr1}p=0} &= 4a\left[\frac{P_{2D}}{K_p}\cdot r^{K_p} + \frac{1}{2}Q_{2D}\cdot r^2\right]_0^{\frac{1}{2}L_{x2D}} \\ \rightarrow F_{\text{GRstr1}p=0} &= a\cdot\left(4\frac{P_{2D}}{K_p}\left(\frac{1}{2}L_{x2D}\right)^{K_p} + \frac{1}{2}Q_{2D}\cdot L_{x2D}^2\right) \end{aligned} \tag{89}$$

and

$$\begin{aligned} F_{\text{GRstr2}p=0} &= 2\gamma H a(s_x - a - L_{x2D}) \quad \text{for } H < \tfrac{1}{2}(s_x - a) \\ F_{\text{GRstr2}p=0} &= 0 \quad \text{for } H \geq \tfrac{1}{2}(s_x - a) \end{aligned} \tag{90}$$

with surcharge load $p > 0$:

$$\begin{aligned} F_{\text{GRstrip:}p>0} = \left(\frac{\gamma H + p}{\gamma H}\right)\cdot\Bigg(&4a\frac{P_{2D}}{K_p}\left(\frac{1}{2}L_{x2D}\right)^{K_p} + \frac{1}{2}aQ_{2D}\cdot L_{x2D}^2 \\ &+ F_{\text{GRstr2}p=0}\Bigg) \end{aligned} \tag{91}$$

For the situation $s_x \neq s_y$ this equations changes into Eq. (14).

A.4. 2D variant: line-shaped support

The 2D equations can be worked out easily for the situation in which the embankment is supported by line-shaped supporting elements (such as diaphragm walls). In this case, Eq. (86) is applicable, where $p_{\text{transferred}} = 0$ kPa, as this is the load transferred from the 3D hemispheres that do not exist in the 2D case.

The total load in kN/m′ on a 1-m-wide line foundation is (in accordance with Eq. (87)):

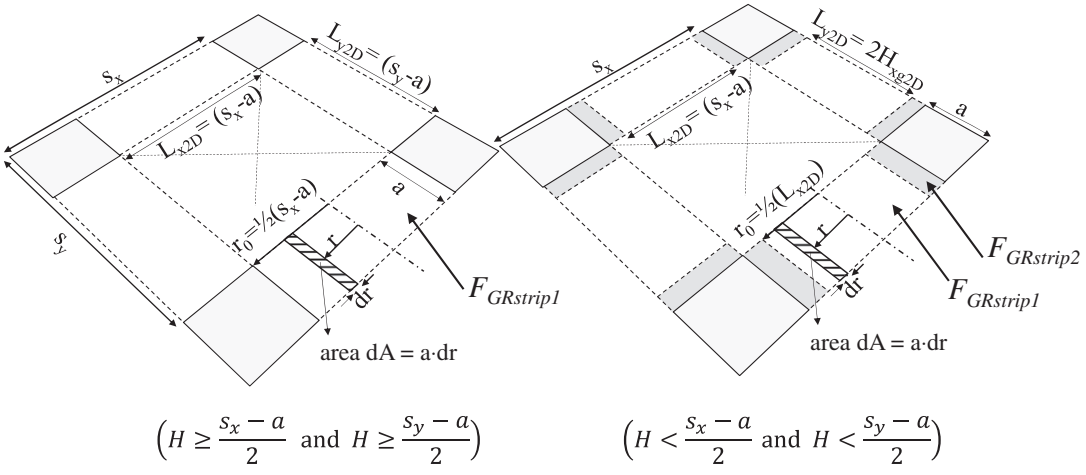

Fig. 23. Integrating the tangential stress σ_θ across the area of the GR strip where the 2D arches exert their load.

$$F_{GR\ line} = F_{GR\ line1} + F_{GR\ line2} = \left(\frac{\gamma H + p}{\gamma H}\right)\cdot\left(F_{GR\ line1p=0} + F_{GR\ line2p=0}\right) \quad (92)$$

where

$$F_{GR\ line1p=0} = 2\int_0^{r_0}\sigma_\theta \mathrm{d}A_{GR\ line} = 2\int_0^{r_0}\sigma_\theta\cdot\mathrm{d}r = 2\int_0^{\frac{1}{2}L_{x2D}}\left(P_{2D}\cdot r^{(K_p-1)} + Q_{2D}\cdot r\right)\mathrm{d}r \quad (93)$$

thus

$$F_{GR\ line1p=0} = 2\left[\frac{P_{2D}}{K_p}\cdot r^{K_p} + \frac{1}{2}Q_{2D}\cdot r^2\right]_0^{\frac{1}{2}L_{x2D}} \rightarrow F_{GR\ line1p=0} = 2\frac{P_{2D}}{K_p}\left(\frac{1}{2}L_{x2D}\right)^{K_p} + \frac{1}{4}Q_{2D}\cdot L_{x2D}^2 \quad (94)$$

and

$$F_{GR\ line2p=0} = \gamma H(s_x - a - L_{x2D}) \quad \text{for } H < \tfrac{1}{2}(s_x - a)$$
$$F_{GR\ line2p=0} = 0 \quad \text{for } H \geq \tfrac{1}{2}(s_x - a) \quad (95)$$

with surcharge load $p > 0$:

$$F_{GR\ line;p>0} = \left(\frac{\gamma H + p}{\gamma H}\right)\cdot\left(2\frac{P_{2D}}{K_p}\left(\frac{1}{2}L_{x2D}\right)^{K_p} + \frac{1}{4}Q_{2D}\cdot L_{x2D}^2 + F_{GR\ line2p=0}\right) \quad (96)$$

Appendix B. Calculation example: the Woerden field test of Fig. 16b

Input parameters			
Diameter circular pile cap	d	0.85	m
Height embankment	H	1.86	m
Lateral ctc distance piles	s_x	2.25	m
Longitudinal ctc distance piles	s_y	2.25	m
Unit weight	γ	18.3	kN/m^3
Surcharge load	p	5	kPa
Cohesion	c	0	kPa
Internal friction angle	φ	43	deg

Calculated parameters				Equation
Equivalent width pile cap	$a = B_{ers}$	0.75	m	$a = \sqrt{\frac{1}{4}\pi d^2}$
Passive earth pressure coefficient	K_p	5.29	–	(2)
Height 3D hemisphere	H_{g3D}	1.59	m	(4)
Width square loaded by 3D arches (Fig. 22)	L_{x3D}	1.50	m	(8)
Length of GR strip loaded by 2D arches (Fig. 23)	L_{x2D}	1.50	m	(12)
Calculation parameter	P_{2D}	90.62	kPa/m^{Kp-1}	(14)
Calculation parameter	Q_{2D}	29.43	kN/m^3	(14)
Calculation parameter	P_{3D}	0.11	kPa/m^{2Kp-2}	(7)
Calculation parameter	Q_{3D}	12.77	kN/m^3	(7)

Determination of the force exerted by the 3D hemispheres on the GR square (no surcharge load yet: $p = 0$)

Force inside circle in GR square (Fig. 22)	$F_{GRsq1;p=0}$	11.21	kN/pile	(6)
Part 1 of force on area inside $L_{x3D}\cdot L_{x3D}$ square, but outside circle (Fig. 22)	$_1F_{GRsq2}$	0.11	kN/pile	(6)
Part 2 of force on area inside $L_{x3D}\cdot L_{x3D}$ square, but outside circle (Fig. 22)	$_2F_{GRsq2}$	20.50	kN/pile	(6)
Part 3 of force on area inside $L_{x3D}\cdot L_{x3D}$ square, but outside circle (Fig. 22)	$_3F_{GRsq2}$	−0.10	kN/pile	(6)
Part 4 of force on area inside $L_{x3D}\cdot L_{x3D}$ square, but outside circle (Fig. 22)	$_4F_{GRsq2}$	−15.33	kN/pile	(6)
Total force on area inside $L_{x3D}\cdot L_{x3D}$ square, but outside circle (Fig. 22)	$F_{GRsq2;p=0}$	5.19	kN/pile	$_1F_{GRsq2} + {}_2F_{GRsq2} + {}_3F_{GRsq2} + {}_4F_{GRsq2}$ (6)
Force on area outside $L_{x3D}\cdot L_{x3D}$ square, but inside GR square)	$F_{GRsq3;p=0}$	0.00	kN/pile	(9)
Total force on GR square (Fig. 22)	$F_{GRsquare;p=0}$	16.40	kN/pile	(6)

Determination of the force transferred along the 3D hemispheres to the 2D arches; to be applied as surcharge load on the 2D arches.

Force transferred	$F_{transferred}$	59.85	kN/pile	(10)
Resulting surcharge load on 2D arches	$p_{transferred}$	21.20	kPa	(11)

Determination of the force exerted by the 2D arches on the GR strips (no surcharge load yet: $p = 0$) and no load outside the arches on the GR strip (Eq. (14))

Total force on GR strips	$F_{GRstrips;p=0}$	35.97	kN/pile	(14)

Determination of load distribution (no surcharge load yet: $p = 0$).

*t*otal force on GR for $p = 0$	$F_{GR} = B + C$	52.37	kN/pile	(16)
Total force on pile cap with $p = 0$	A	119.94[a]	kN/pile	(15)

[a] This is the value given in Fig. 16b.

Determination of load distribution (with surcharge load: $p = 5$ kPa).

Total force on GR for $p = 5$ kPa	$F_{GR} = B + C$	61.60	kN/pile	(16)
Total force on pile cap for $p = 5$ kPa	A	141.09	kN/pile	(15)
Total pressure on pile cap for $p = 5$ kPa	p_A	248.63	kPa	$p_A = A/A_p$
Percentage of total force transferred to the pile cap directly for $p = 5$ kPa	$A\%$	69.6	%	$A\% = A/((\gamma H + p)^* s_x^2)$

Step 2 with the inverse triangular load distribution according to Van Eekelen et al. (2012b).

Additional parameters:

Subgrade reaction	k	0.00	kN/m^3
GR stiffness[b]	J	5000	kN/m

[b] Stress and time dependent. The GR stiffness should be determined from isochronic curves.

The average geometric and constitutive strains should be equalised numerically:

$$\frac{\mathrm{d}x\sum_{x=0}^{x=\frac{1}{2}(s_x-a)}\left(\sqrt{1+\left(\frac{\mathrm{d}z}{\mathrm{d}x}\right)^2}\right)-\frac{1}{2}(s_x-a)}{\frac{1}{2}(s_x-a)}=\mathrm{d}x\sum_{x=0}^{x=\frac{1}{2}(s_x-a)}\left(\frac{T(x)}{J}\right) \quad (97)$$

We find:

Max GR deflection	$z(x=0)$	0.022	m	Van Eekelen et al., 2012b, Eq. (15)
GR inclination at edge pile cap	$\mathrm{d}z/\mathrm{d}x$ at $x=½(s_x-a)$	−0.332	m/m	Van Eekelen et al., 2012b, Eq. (15)
Average GR strain	$\varepsilon_{average}$	0.582	%	Van Eekelen et al., 2012b, Eq. (18) with correction given in Eq. (97) of this paper
Max GR strain at the edge of the pile cap	ε_{max} at $x=½(s_x-a)$	0.609	%	Van Eekelen et al., 2012b, Eq. (15)
Max tensile force at the edge of the pile cap	T_{max} at $x=½(s_x-a)$	30.5	kN/m	Van Eekelen et al., 2012b, Eq. (15)

Appendix of Analytical model for arching in piled embankments

References

Abusharar, S.W., Zeng, J.J., Chen, B.G., Yin, J.H., 2009. A simplified method for analysis of a piled embankment reinforced with geosynthetics. Geotextiles and Geomembranes 27, 39–52.

ASIRI, 2012. Recommandations pour la conception, le dimensionnement, l'exécution et le contrôle de l'amélioration des sols de fondation par inclusions rigides, ISBN 978-2-85978-462-1.

Blanc, M., Rault, G., Thorel, L., Almeida, M., 2013. Centrifuge investigation of load transfer mechanisms in a granular mattress above a rigid inclusions network. Geotextiles and Geomembranes 36, 92–105.

BS8006-1, 2010. Code of Practice for Strengthened/reinforced Soils and Other Fills. British Standards Institution, ISBN 978-0-580-53842-1.

Britton, E., Naughton, P., 2008. An experimental investigation of arching in piled embankments. In: Proceedings of the 4th European Geosynthetics Congress EuroGeo 4. Edinburgh. Paper number 106.

Cain, W., 1916. Earth Pressure, Retaining Walls and Bins. John Wiley and Sons. Inc., New York.

Carlsson, B., 1987. Reinforced Soil, Principles for Calculation. Terratema AB, Linköping (in Swedish).

Casarin, C., 2011. Private Communication, São Paulo, Brazil.

Chen, R.P., Chen, Y.M., Han, J., Xu, Z.Z., 2008. A theoretical solution for pile-supported embankments on soft soils, under one-dimensional compression. Canadian Geotechnical Journal 45, 611–623.

Chen, Y.M., Cao, W.P., Chen, R.P., 2008. An experimental investigation of soil arching within basal reinforced and unreinforced piled embankments. Geotextiles and Geomembranes 26, 164–174.

Collin, J.G., 2004. Column supported embankment design considerations. In: 52nd Annual Geotechnical Engineering Conference. University of Minnesota.

CUR 226, 2010. Ontwerprichtlijn paalmatrassystemen (Design Guideline Piled Embankments), ISBN 978-90-376-0518-1 (in Dutch).

Deb, K., Mohapatra, S.R., 2012. Analysis of stone column-supported geosynthetic-reinforced embankments. Applied Mathematical Modelling.

Deb, K., 2010. A mathematical model to study the soil arching effect in stone column-supported embankment resting on soft foundation soil. Applied Mathematical Modelling 34, 3871–3883.

Den Boogert, Th., Van Duijnen, P.G., Van Eekelen, S.J.M., 2012. Numerical analysis of geosynthetic reinforced piled embankent scale model tests. Plaxis Bulletin 31, 12–17.

EBGEO, 2010. Empfehlungen für den Entwurf und die Berechnung von Erdkörpern mit Bewehrungen aus Geokunststoffen e EBGEO, vol. 2. German Geotechnical Society, Auflage, ISBN 978-3-433-02950-3 (in German). Also available in English: Recommendations for Design and Analysis of Earth Structures using Geosynthetic Reinforcements e EBGEO, 2011. ISBN: 978-3-433-02983-1 and digital in English ISBN: 978-3-433-60093-1.

Ellis, E., Aslam, R., June 2009. Arching in piled embankments. Comparison of centrifuge tests and predictive methods, part 1 of 2. Ground Engineering, 34–38.

Eskişar, T., Otani, J., Hironaka, J., 2012. Visualization of soil arching on reinforced embankment with rigid pile foundation using X-ray CT. Geotextiles and Geomembranes 32, 44–54.

Filz, G.M., Sloan, J.A., McGuire, M.P., Collin, J.G., Smith, M.E., 2012. Column-supported embankments: settlement and load transfer. In: Proceedings of Geo-Congress, Oakland, California, March, p. 24.

Filz, G., Sloan, J., 2013. Load distribution on geosynthetic reinforcement in column-supported embankments. In: Proceedings of Geo-congress, March 2013, California.

Guido, V.A., Kneuppel, Sweeney, M.A., 1987. Plate loading test on geogrid reinforced earth slabs. In: Proceedings Geosynthetics'87 Conference, New Orleans, pp. 216–225.

Han, J., Gabr, M.A., January 2002. Numerical analysis of geosynthetic-reinforced and pile-supported earth platforms over soft soil. Journal of Geotechnical and Geoenvironmental Engineering 44, 44–51.

Han, J., Bhandari, A., Wang, F., 2012. DEM analysis of stresses and deformations of geogrid-reinforced embankments over piles. International Journal of Geomechanics 12, 340–350.

Handy, R.L., March, 1985. The arch in soil arching. Journal of Geotechnical Engineering III (3). ©ASCE, ISSN: 0733-9410/85/0003-0302/$01.00. Paper No. 19547.

Hewlet, W.J., Randolph, M.F., April 1988. Analysis of piled embankments. Ground Engineering 22 (3), 12–18.

Hong, W.P., Lee, J.H., Lee, K.W., 2007. Load transfer by soil arching in pile-dupported embankments. Soils and Foundations 47 (5), 833–843.

Jenck, O., Dias, D., Kastner, R., 2009. Discrete element modelling of a granular platform supported by piles in soft soil – validation on a small scale model test and comparison to a numerical analysis in a continuum. Computers and Geotechnics 36, 917–927.

Jones, C.J.F.P., Lawson, C.R., Ayres, D.J., 1990. Geotextile reinforced piled embankments. In: Hoedt, Den (Ed.), Geotextiles, Geomembranes and Related Products. Balkema, Rotterdam, ISBN 90 6191 119 2, pp. 155–160.

Kempfert, H.-G., Göbel, C., Alexiew, D., Heitz, C., 2004. German recommendations for reinforced embankments on pile-similar elements. In: Proceedings of EuroGeo 3, Munich, pp. 279–284.

Lally, D., Naughton, P.J., 2012. An investigation of the arching mechanism in a geotechnical centrifuge. In: Proceedings 5th European Geosynthetics Congress. Valencia, vol. 5, pp. 363–367.

Le Hello, B., Villard, P., 2009. Embankments reinforced by piles and geosynthetics – numerical and experimental studies with the transfer of load on the soil embankment. Engineering Geology 106, 78–91.

Liikenneviraston, 2012. Geolujitetut maarakenteet, Tiegeotekniikan käsikirja, Liikenneviraston oppaita 2/2012, ISBN 978-952-255-104-7. Finnish design guideline for geosynthetic reinforcement (in Finnish).

Marston, A., Anderson, A.O., 1913. The Theory of Loads on Pipes in Ditches and Tests of Cement and Clay Drain Tile and Sewer Pipe. Bulletin No. 31. Engineering Experiment Station.

McGuire, M., Sloan, J., Collin, J., Filz, G., 2012. Critical height of column-supported embankments from Bench-Scale and field-scale tests. In: TC 211 International Symposium on Ground Improvement IS-GI Brussels. ISSMGE.

McKelvey, J.A., 1994. The anatomy of soil arching. Geotextiles and Geomembranes 13, 317–329.

Naughton, P., 2007. The significance of critical height in the design of piled embankments. Soil Improvement, 1–10. http://dx.doi.org/10.1061/40916(235)3.

Nadukuru, S.S., Michalowski, R.L., May 2012. Arching in distribution of active load on retaining walls. Journal of Geotechnical and Geoenvironmental Engineering, 575–584.

Public Work Research Center, 2000. Manual on Design and Execution of Reinforced Soil Method with Use of Geotextiles, second ed. Public Work Research Center, pp. 248–256. (in Japanese).

Rogbeck, Y., Gustavsson, S., Södergren, I., Lindquist, D., 1998. Reinforced piled embankments in Sweden – design aspects. In: Proceedings of the Sixth International Conference on Geosynthetics, pp. 755–762.

Russell, D., Pierpoint, N., November 1997. An assessment of design methods for piled embankments. Ground Engineering, 39–44.

SINTEF, 2002. A computer program for designing reinforced embankments. In: Proc. 7th International Conference on Geotextiles, Nice 2002, France, vol. 1, pp. 201–204.

Sloan, J.A., 2011. Column-supported embankments: full-scale tests and design recommendations. PhD thesis, Faculty of the Virginia Polytechnic Institute of State University, Blacksburg, VA, USA.

Svanø, G., Ilstad, T., Eiksund, G., Want, A., 2000. Alternative calculation principle for design of piled embankments with base reinforcement. In: Proceedings of the 4th GIGS in Helsinki.

Terzaghi, K., 1943. Theoretical Soil Mechanics. John Wiley and Sons, New York.

Van Duijnen, P.G., Van Eekelen, S.J.M., Van der Stoel, A.E.C., 2010. Monitoring of a railway piled embankment. In: Proceedings of 9 ICG, Brazil, pp. 1461–1464.

Van Eekelen, S.J.M., Bezuijen, A., Oung, O., 2003. Arching in piled embankments; experiments and design calculations. In: Proceedings of Foundations: Innovations, Observations, Design and Practice, pp. 885–894.

Van Eekelen, S.J.M., Jansen, H.L., Van Duijnen, P.G., De Kant, M., Van Dalen, J.H., Brugman, M.H.A., Van der Stoel, A.E.C., Peters, M.G.J.M., 2010. The Dutch design guideline for piled embankments. In: Proceedings of 9 ICG, Brazil, pp. 1911–1916.

Van Eekelen, S.J.M., Bezuijen, A., Van Tol, A.F., 2011. Analysis and modification of the British Standard BS8006 for the design of piled embankments. Geotextiles and Geomembranes 29, 345–359.

Van Eekelen, S.J.M., Bezuijen, A., Lodder, H.J., van Tol, A.F., 2012a. Model experiments on piled embankments Part I. Geotextiles and Geomembranes 32, 69–81.

Van Eekelen, S.J.M., Bezuijen, A., Lodder, H.J., van Tol, A.F., 2012b. Model experiments on piled embankments. Part II. Geotextiles and Geomembranes 32, 82–94 (including its corrigendum Van Eekelen, S.J.M., Bezuijen, A., Lodder, H.J., van Tol, A.F., 2012b2. Corrigendum to 'Model experiments on piled embankments. Part II' [Geotextiles and Geomembranes 32 (2012) pp. 82–94]. Geotextiles and Geomembranes 35: 119).

Van Eekelen, S.J.M., Bezuijen, A., 2012. Does a piled embankment 'feel' the passage of a heavy truck? High frequency field measurements. In: Proceedings of the 5th European Geosynthetics Congress EuroGeo 5. Valencia. Digital version, vol. 5, pp. 162–166.

Van Eekelen, S.J.M., Bezuijen, A., 2013. Dutch research on piled embankments. In: Proceedings of Geo-Congress, California, March 2013.

Vermeer, P.A., Punlor, A., Ruse, N., 2001. Arching effects behind a soldier pile wall. Computers and Geotechnics 28, 379–396.

Völlmy, A., 1937. Eingebettete Rohre, Mitt. Inst. Baustatik, Eidgen. Tech. Hochschule, Zürich, Mitt. No. 9.

Zaeske, D., February 2001. Zur Wirkungsweise von unbewehrten und bewehrten mineralischen Tragschichten über pfahlartigen Gründungselementen. Schriftenreihe Geotechnik, Uni Kassel. Heft 10 (in German).

Zhang, L., Zhao, M., Hu, Y., Zhao, H., Chen, B., June 2012. Semi-analytical solutions for geosynthetic-reinforced and pile-supported embankment. Computers and Geotechnics. ISSN: 0266-352X 44, 167–175. http://dx.doi.org/10.1016/j.compgeo.2012.04.001.